Control Engineering Practice 177 (2026) 107206

Contents lists available at ScienceDirect

Control Engineering Practice

journal homepage: www.elsevier.com/locate/conengprac

An energy flow control strategy for the secondary lateral semi-active suspension of metro vehicles

Xinmiao Chen, Yuan Yao*, Haifeng Xie

State Key Laboratory of Rail Transit Vehicle System, Southwest Jiaotong University, Chengdu, China

ARTICLE INFO

Keywords:
Metro vehicles
Semi-active suspension
MR damper
Hardware-in-the-loop tests

ABSTRACT

Low frequency lateral carbody vibration has been observed on several metro lines in China, reducing ride comfort. This study investigates a secondary lateral semi-active suspension for metro vehicles and analyzes how it affects carbody vibration from the perspective of power and energy flow. This analysis shows that the controllable damper has two related effects: it can regulate the variation of carbody kinetic energy, and it can weaken the vibration power transmitted from the bogie frame to the carbody. Based on this interpretation, semi-active control is viewed as a coordinated balance between regulating carbody kinetic energy and isolating the carbody from the bogie-frame vibration transmitted through the suspension. An energy flow control (EFC) strategy is then developed, in which an energy flow allocation factor is introduced to coordinate these two control tendencies. A full vehicle co-simulation model is established, and HIL tests with physical MR dampers are conducted for validation. Results under four combined operating conditions (LM wheel and worn LM wheel profiles at 80 km/h and 100 km/h) show that EFC improves the lateral Sperling index while maintaining relatively low carbody jerk and suspension deflection.

1. Introduction

Low frequency carbody swaying vibration has been reported on several urban rail transit lines in China. This problem not only reduces ride comfort and causes passenger complaints, but also increases the maintenance burden on the wheel–rail system and suspension components. On one metro line, the lateral Sperling index of the carbody exceeded 4.0 when the speed reached around 80 km/h, far above the "excellent" threshold of 2.5 (Li et al., 2025). Existing studies have shown that changes in wheel–rail conditions and operating speed strongly affect low-frequency lateral vibration (Jiang et al., 2025; Shi et al., 2020). In engineering practice, wheel reprofiling and passive suspension parameter adjustments remain the main countermeasures. However, these methods rely heavily on experience. They also struggle to maintain ride quality and keep maintenance costs low under varying speeds and different wheel–rail matching conditions. As a result, their long-term effectiveness is limited.

Compared with passive suspension, semi-active suspension allows the damping coefficient to be adjusted. In some cases, it can achieve vibration reduction close to that of active suspension while keeping energy consumption low and offering better engineering practicability. This makes it a promising solution for the above problem. Its key actuators include adjustable damping devices such as electro-hydraulic dampers (Ma et al., 2019) and MR dampers (Fu & Bruni, 2022). Among these, the MR damper stands out for its fast response, wide controllable force range, and relatively simple structure. It has been widely used in automotive suspension systems (Soliman & Kaldas, 2021), and its application in railway vehicles is also gaining interest. For urban rail vehicles, whose operating conditions vary markedly while maintenance cost constraints remain stringent, the secondary lateral semi-active suspension is particularly suitable. It offers a practical way to reduce vibration and improve adaptability under existing wheel–rail and track conditions, without relying on a single fixed passive damping parameter.

Research on semi-active suspension control has followed several lines, including classical methods, model-based methods, and intelligent or data-driven approaches. Among the classical ones, Sky-hook (SH) and acceleration-driven damper (ADD) control are widely studied for their clear physical interpretation. Building on them, SH-ADD combines the advantages of SH and ADD to reduce vehicle vibration acceleration over the full frequency range (Savaresi & Spelta, 2007). SH-PDD combines SH and PDD(power-driven-damper) through a switching law based on the difference between the squared velocities of the sprung and unsprung masses, achieving effective vibration reduction over a wide frequency range (Liu & Zuo, 2016). Other mixed or extended strategies have been proposed to meet vibration reduction needs across different frequency ranges (Lu et al., 2023; Zhang & Chen, 2025). A road condition

* Corresponding author.
E-mail address: yyuan@swjtu.edu.cn (Y. Yao).

https://doi.org/10.1016/j.conengprac.2026.107206
Received 5 May 2026; Received in revised form 13 July 2026; Accepted 6 August 2026
Available online 14 August 2026
0967-0661/© 2026 Elsevier Ltd. All rights are reserved, including those for text and data mining, AI training, and similar technologies.

adaptive semi-active suspension control method was developed by combining LSTM-based road identification with a self-tuning fuzzy sliding mode controller (Jiang et al., 2024), and a decentralized modular semi-active control framework was proposed for vibration suppression and energy harvesting (Pisarski & Jankowski, 2024). In the field of predictive control, while a multi-model preview controller has been developed for real semi-active suspension systems (Achnib & Sename, 2023), an MPC-based controller is specifically adopted to preview road information and compensate for delays (Kim et al., 2023). Beyond these, deep-learning-based semi-active control (Lee et al., 2023) and frequency domain control strategies that offer hardware cost advantages (Wang et al., 2026) also show good potential for engineering application.

In the railway field, researchers have explored sliding mode control (Shi et al., 2024), fuzzy control (Zhang et al., 2023b), neural network control (Ghoniem et al., 2020), fractional order control (Zolotas & Goodall, 2018), model-based LQR and MPC (Fu et al., 2024), and $H\infty/H_2$ robust control (Zong et al., 2013). Their effectiveness has been verified through simulation or experiments. Overall, these studies show that semi-active suspension has clear potential for improving the vibration performance of railway vehicles. However, the problem is not simply about finding a controller that works. Railway vehicles have strong nonlinear characteristics, and changes in wheel–rail contact conditions can significantly alter their dynamic behavior. This poses a serious challenge for model-based control strategies (Zhang et al., 2023a). Most existing studies focus mainly on control performance itself, while the physical mechanism behind the control action is discussed less thoroughly. In particular, it remains unclear why control dominated by velocity feedback performs better under some conditions, whereas strategies relying mainly on acceleration feedback become preferable under others, and why mixed strategies usually provide superior performance over a wider frequency range. These questions still lack a unified and clear physical explanation.

Transfer-function-based methods, including frequency-response, phase-response, and Bode analyses, are widely used in control-system studies. They are effective for evaluating vibration response in different frequency ranges, and comparing the dynamic performance of different control strategies. These methods provide a clear input-output description of the controlled system and are especially useful for analyzing linearized models and frequency-dependent control effects. In this study, the application of semi-active suspension to railway vehicles is further examined from an energy-flow perspective. Energy-based viewpoints have been widely used to describe vibration control systems because they can relate control actions to energy storage, dissipation, and power transmission. For example, port-Hamiltonian (Morselli & Zanasi, 2008; Zhu & Ying, 2013) and related energy-flow formulations provide useful theoretical tools for interpreting energy exchange in controlled mechanical systems. This study uses an energy-flow interpretation based on the semi-active damping force, carbody kinetic energy, and suspension-transmitted power to explain the different roles of classical semi-active strategies and to motivate the proposed EFC strategy.

Experimental validation is also needed for semi-active suspension research. Existing test methods for semi-active suspension of railway vehicles include field tests, rolling and vibration test rigs (Wu et al., 2023), scaled model tests (Jin et al., 2020), and hardware-in-the-loop (HIL) tests (Liu et al., 2022). Field tests and rolling and vibration test rigs offer high fidelity, but they are costly and time-consuming. Scaled model tests have advantages in cost and controllability. HIL testing can introduce both physical actuators and the actual controller implementation at a lower cost, making it an important validation tool in semi-active suspension research (Yang et al., 2023). However, most existing HIL studies still rely on vehicle models with few degrees of freedom, making it difficult to balance model accuracy and real-time performance. To more realistically evaluate controller performance under a more detailed vehicle model, a HIL platform that combines a full vehicle multibody dynamics model with a physical MR damper is still needed.

(a) Metro vehicle.

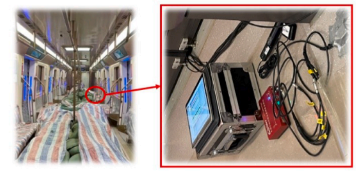

(b) Acceleration sensor on floor of front aisle.

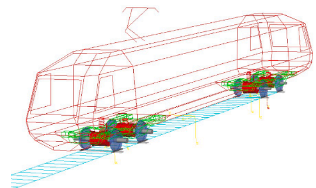

(c) Vehicle dynamic model in SIMPACK.

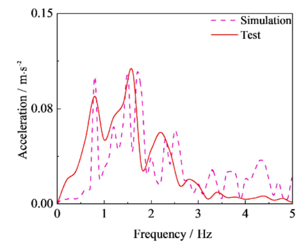

(d) Frequency domain response at the front aisle floor of the carbody.

Fig. 1. Field experiments, vehicle model, and validation results.

Against this background, the study investigates the secondary semi-active suspension of a metro vehicle with permanent magnet direct drive motors and inboard bogies. The main contributions are summarized as follows:

1. An energy-flow interpretation of secondary lateral semi-active suspension is developed based on the power interaction among the carbody, secondary suspension, and bogie frame. It explains the roles of classical semi-active strategies from the viewpoint of carbody kinetic-energy regulation and suspension-input isolation.
2. An energy flow control (EFC) strategy is proposed with a fractional order shaping branch and an energy flow allocation factor. It achieves coordination between regulating the carbody kinetic energy and isolating the carbody from bogie-frame vibration transmitted through the suspension.
3. A full-vehicle co-simulation model and a HIL test platform are built. The platform combines the SIMPACK full-vehicle model, physical MR dampers, and a real-time controller. The proposed strategy is evaluated under different wheel profiles and speeds.

2. Vehicle models and evaluation indices

2.1. Full vehicle multibody dynamics model

The vehicle investigated in this study is an A-type metro vehicle with a permanent magnet direct drive motor and an inboard bogie. This paper focuses on the influence of the secondary lateral suspension on carbody lateral vibration. The service speed of this vehicle is 80 km/h.

To obtain the dynamic characteristics of the vehicle under representative operating conditions, field tests were conducted on a fully loaded vehicle fitted with reprofiled wheelsets (LM profile), and the test speed was approximately 70 km/h. Lateral vibration acceleration sensors were mounted on the front floor of the carbody, as shown in Fig. 1(a) and (b). The accelerometers had a measurement range of ±2 g, and the sampling frequency was 2000 Hz.

Based on the parameters of the tested vehicle, a full vehicle multibody dynamics model was established in SIMPACK, as shown in Fig. 1(c). The vehicle was modeled as a rigid multibody system. The model comprises one carbody, two bogie frames, four wheelsets, four traction motors, and eight axle-box assemblies. The primary suspension connects the axle-box assemblies to the bogie frames and the secondary suspension connects the bogie frames to the carbody. The traction motors are mounted on the bogie frame through an elastic sus-

Table 1
Vehicle dynamic model parameters.

Parameters	Value	Unit
Mass of carbody	40.1×10^3	kg
Roll inertia of carbody	71.5×10^3	kg·m^2
Yaw inertia of carbody	1.71×10^6	kg·m^2
Pitch inertia of carbody	1.75×10^6	kg·m^2
Mass of bogie frame	3.8×10^3	kg
Roll inertia of bogie frame	551.3	kg·m^2
Yaw inertia of bogie frame	2.5×10^3	kg·m^2
Pitch inertia of bogie frame	2.1×10^3	kg·m^2
Mass of wheelset	1.25×10^3	kg
Mass of motor	0.83×10^3	kg
Secondary lateral stiffness	0.38×10^6	N/m
Secondary longitudinal stiffness	0.38×10^6	N/m
Secondary vertical stiffness	0.41×10^6	N/m
Secondary vertical damping	30×10^3	N·s/m
Primary lateral stiffness	14.1×10^6	N/m
Primary longitudinal stiffness	14.1×10^6	N/m
Primary vertical stiffness	4.6×10^6	N/m
Primary vertical damping	6.55×10^3	N·s/m

pension arrangement. The carbody, bogie frames, wheelsets, and traction motors were each assigned six degrees of freedom. The main model parameters are listed in Table 1. Both the primary and secondary suspension systems were represented by spring–damper elements. Simulation was carried out using the measured track spectrum and CHN60 rails. The wheel profile was set as the standard LM profile, whose equivalent conicity is 0.1 under the considered wheel–rail matching condition. The simulated lateral acceleration spectrum at the front floor of the carbody is compared with the measured result from the field test, as shown in Fig. 1(d). The simulated and measured spectra show similar dominant frequency components and comparable amplitude levels at the front floor of the carbody. This agreement indicates that the model can reproduce the main lateral vibration characteristics observed in the field test. Therefore, the model is considered suitable for comparing different secondary lateral semi-active control strategies.

The SIMPACK full-vehicle multibody dynamic model is used as the main model for performance evaluation and HIL analysis, whereas the simplified model introduced later is used only for control mechanism interpretation. Modal analysis of the full-vehicle model shows that the low-frequency lateral-related carbody modes include lower sway, yawing and upper sway modes, with frequencies of approximately 0.50 Hz, 0.85 Hz and 1.42 Hz, respectively.

2.2. Half-vehicle lateral model

To further analyse the energy transfer in the secondary lateral semi-active suspension, a half-vehicle lateral model is established, as shown in Fig. 2. This simplified model is introduced to extract the main lateral dynamic relationship among the carbody, secondary suspension, bogie frame, and wheelset. It provides a clear object for interpreting the energy-flow-based control law.

Here, m_c, m_f and m_w denote the carbody mass (20×10^3 kg), the bogie frame mass (3.8×10^3 kg) and the wheelset mass (1.25×10^3 kg), respectively. k_s denotes the secondary lateral stiffness (3.8×10^5 N/m). k_p denotes the primary lateral stiffness (28.2×10^6 N/m). k_{gy} denotes the equivalent wheel–rail lateral stiffness (20×10^6 N/m). The wheelbase l is 2.1 m, and the running speed v is 80 km/h. f_{22} denotes the lateral creep coefficient (9.98×10^6 N/m). $c_s(t)$ denotes the secondary lateral damper coefficient with $c_s(t)\in[c_{\min},c_{\max}]$, where $c_{\max}$, $c_{\min}$ denote the maximum and minimum damping coefficients, respectively. y_c, y_f, y_w and y_r represent the carbody displacement, bogie frame displacement, wheelset displacement and track excitation displacement, respectively. The model differential equations are formulated as follows.

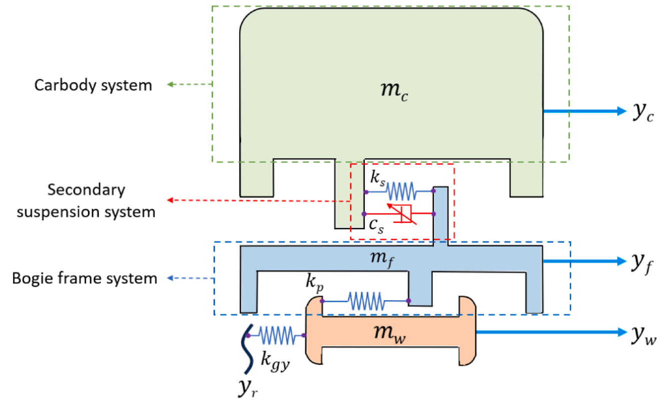

Fig. 2. Half-vehicle lateral model.

$$\begin{cases} m_c\ddot{y}_c = -k_s(y_c-y_f) - c_s(t)(\dot{y}_c-\dot{y}_f), \\ m_f\ddot{y}_f = k_s(y_c-y_f) + c_s(t)(\dot{y}_c-\dot{y}_f) - k_p(y_f-y_w), \\ m_w\ddot{y}_w = k_p(y_f-y_w) - 2f_{22}\dot{y}_w/v + k_{gy}(y_r-y_w), \quad i=1,2, \\ y_{r2}(t) = y_{r1}\left(t-\dfrac{l}{v}\right). \end{cases} \tag{1}$$

2.3. Evaluation indices

Three indices are used to evaluate the control performance of the secondary lateral semi-active suspension: the lateral Sperling index, the RMS value of the carbody lateral jerk, and the RMS value of the secondary suspension dynamic deflection. The lateral Sperling index is used as the main ride-quality indicator. The jerk describes the sharpness of the carbody acceleration variation caused by damping adjustment and control-force fluctuation, while the suspension dynamic deflection reflects the motion constraint of the secondary suspension.

The first evaluation index adopted is the lateral Sperling index of the carbody. According to the Chinese standard GB/T 5599-2019 (GB/T, 2019), this index is calculated by weighting the carbody floor acceleration at different frequencies and taking the sum of the weighted values. It is defined as follows:

$$W = 3.57\sqrt[10]{\frac{A^3}{f}F(f)}. \tag{2}$$

Here, A denotes the acceleration, f denotes the vibration frequency, and $F(f)$ denotes the frequency weighting factor.

The second index is the root mean square (RMS) value of the lateral jerk at the carbody suspension mounting point. In the following text, “carbody jerk” refers to the lateral jerk measured at this point. Some control strategies may introduce high-frequency chattering, which may increase the loading demand on the damper, mounting joints, and connecting components.

$$W_{\dddot{y}_c} = \sqrt{\frac{1}{N}\sum_{i=1}^{N}\dddot{y}_{c,i}^2}. \tag{3}$$

Here, N denotes the number of sampling points, and $\dddot{y}_c$ denotes the carbody jerk.

The third index is the RMS value of the secondary suspension dynamic deflection. According to the relevant Chinese standard (CJJ/T, 2018), the secondary suspension displacement is subject to a specified limit. Suspension deformation also affects structural clearance. Larger suspension deformation may reduce the available lateral clearance and increase the possibility of bumpstop contact.

$$W_{\Delta y_{cf}} = \sqrt{\frac{1}{N}\sum_{i=1}^{N}\Delta y_{cf,i}^2}. \tag{4}$$

Here, N denotes the number of sampling points, and Δy_{cf} denotes the suspension dynamic deflection. The subsequent descriptions of suspension displacement all refer to the suspension dynamic deflection.

The maximum track shift force is also included in the discussion to assess the influence of the semi-active suspension.

3. Energy flow analysis of semi-active control

3.1. Energy flow analysis of secondary lateral suspension systems

For the secondary lateral semi-active suspension considered in this study, the MR damper cannot generate an arbitrary active control force. The controllable variable is the damping coefficient $c_s(t)$, and the corresponding damping force is constrained by the relative velocity and the control current. Therefore, the semi-active damper changes the vehicle vibration response by regulating the power flow and energy transfer through the secondary suspension. To clarify this mechanism, the half-vehicle lateral model shown in Fig. 2 is used for the following energy-flow analysis.

For the energy-flow interpretation of the carbody-secondary suspension-bogie frame chain, the following local stored energy is considered:

$$H(x) = \frac{1}{2}m_c\dot{y}_c^2 + \frac{1}{2}m_f\dot{y}_f^2 + \frac{1}{2}k_s y_{cf}^2. \tag{5}$$

Here, $y_{cf} = y_c - y_f$.

The secondary lateral suspension force is written as:

$$F_s(c_s) = k_s y_{cf} + c_s(t)\dot{y}_{cf}. \tag{6}$$

According to the force direction defined in this study, the instantaneous power input from the secondary suspension to the carbody is

$$P_c(c_s) = -F_s(c_s)\dot{y}_c = -k_s y_{cf}\dot{y}_c - c_s(t)\dot{y}_{cf}\dot{y}_c. \tag{7}$$

The power $P_c(c_s)$ consists of two parts. The first term, $-k_s y_{cf}\dot{y}_c$, is associated with the secondary spring, while the second term, $-c_s\dot{y}_{cf}\dot{y}_c$, is associated with the secondary damper. Since the damping coefficient can be adjusted by the semi-active actuator, the damper term is the controllable part of the power input to the carbody. When ($P_c(c_s)>0$), the secondary suspension inputs energy into the carbody. When ($P_c(c_s)<0$), the secondary suspension absorbs energy from the carbody.

The net power flowing into the secondary suspension is

$$P_s(c_s) = F_s(c_s)\dot{y}_{cf}. \tag{8}$$

Substituting Eq. (6) into Eq. (8) gives

$$P_s(c_s) = k_s y_{cf}\dot{y}_{cf} + c_s(t)\dot{y}_{cf}^2. \tag{9}$$

The net suspension power P_s characterizes the vibration transmission through the secondary suspension. Regulating P_s toward zero weakens the vibration transmitted from the bogie frame to the carbody.

3.2. Analysis of energy flow in semi-active control strategies

Based on the subsystem energy analysis, the classic semi-active control laws can be reinterpreted from an energy flow viewpoint. This analysis shows that classical strategies emphasize different physical effects in the same suspension system.

The Sky-hook (SH) damping control law is given by

$$c_s(t) = \begin{cases} c_{\max}, & \text{if } \dot{y}_c\dot{y}_{cf} > 0, \\ c_{\min}, & \text{otherwise.} \end{cases} \tag{10}$$

The key term in Eq. (7) is the damping-power term $-c_s(t)\dot{y}_{cf}\dot{y}_c$. When $\dot{y}_c\dot{y}_{cf} > 0$, increasing the damping coefficient enhances the negative power exerted on the carbody, which means that more energy can be absorbed from the carbody. In contrast, when $\dot{y}_c\dot{y}_{cf} < 0$, a large damping coefficient tends to increase the positive power input to the carbody. Therefore, the damping coefficient should be switched to the low-damping state.

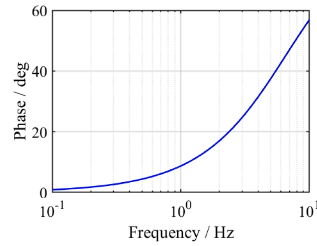

(a) Phase-frequency characteristic between $\dot{y}_c$ and $\dot{y}_{cf}$.

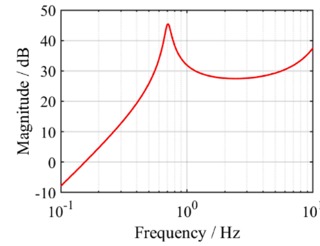

(b) Magnitude-frequency characteristic from y_r to $\dot{y}_c$.

Fig. 3. Frequency-domain characteristics of the half-vehicle model.

The mechanical energy of the carbody subsystem contains only the lateral kinetic energy:

$$H_c = \frac{1}{2}m_c\dot{y}_c^2. \tag{11}$$

Taking the derivative of H_c gives

$$\dot{H}_c = -k_s y_{cf}\dot{y}_c - c_s(t)\dot{y}_{cf}\dot{y}_c. \tag{12}$$

Eq. (12) is equivalent to Eq. (7), namely $\dot{H}_c = P_c(c_s)$. If the carbody kinetic energy is to be reduced, the power input from the secondary suspension to the carbody should be regulated. Let $H_{c,d}$ be the desired level of energy for the carbody system. H_c is positive semidefinite. When the carbody kinetic energy exceeds a reference level $H_{c,d}$, the corresponding control tendency can be expressed as:

$$c_s(t) = \arg\min_{c_s\in\{c_{\min},c_{\max}\}} P_c(c_s), \quad \text{when } H_c > H_{c,d}. \tag{13}$$

This expression means that, when the carbody kinetic energy is high, the controllable damping is adjusted to enhance the negative power exerted by the suspension on the carbody, or equivalently to reduce its positive power input, so that the carbody kinetic energy can decrease more effectively. Accordingly, SH can be interpreted as a semi-active control law that mainly aims at regulating the carbody kinetic energy. When $H_{c,d} = 0$, Eq. (13) becomes consistent with the switching rule in Eq. (10).

Based on Eq. (1), the phase-frequency characteristic between $\dot{y}_c$ and $\dot{y}_{cf}$, and the magnitude-frequency characteristic from y_r to $\dot{y}_c$, are shown in Fig. 3. As shown in Fig. 3(a), the phase difference between $\dot{y}_c$ and $\dot{y}_{cf}$ is small in the low-frequency range. Therefore, during a larger portion of one vibration cycle, the damper can perform negative work on the carbody. Fig. 3(b) shows that the carbody velocity response is large in the low-frequency range, which indicates a high level of carbody kinetic energy. Therefore, in low-frequency vibration, the secondary suspension can more effectively absorb energy from the carbody, reduce the carbody kinetic energy, and improve the carbody vibration behavior. This explains why the control concept of minimizing carbody kinetic energy through power-flow regulation is suitable for low-frequency resonance control.

For the classical ADD control, the control law is

$$c_s(t) = \begin{cases} c_{\max}, & \text{if } \ddot{y}_c\dot{y}_{cf} > 0, \\ c_{\min}, & \text{otherwise.} \end{cases} \tag{14}$$

After substituting the system dynamics in Eq. (1) and Eq. (9), one obtains

$$\ddot{y}_c\dot{y}_{cf} = -\frac{P_s(c_s)}{m_c}. \tag{15}$$

Thus, the ADD can be further written as

$$c_s(t) = \begin{cases} c_{\max}, & \text{if } P_s(c_s) < 0, \\ c_{\min}, & \text{otherwise.} \end{cases} \tag{16}$$

Since the damping-related term $c_s \dot{y}_{cf}^2$ in $P_s(c_s)$ is non-negative, the ADD law can be interpreted as selecting the damping coefficient to make the net power of the secondary suspension approach a prescribed reference. Let $P_{s,d}$ be the desired net power entering the secondary suspension system. The relevant quantity is the instantaneous power $P_s(c_s)$ from Eq. (9). The corresponding isolation-oriented control tendency can be expressed as

$$c_s(t) = \arg \min_{c_s \in \{c_{\min}, c_{\max}\}} \left| P_s(c_s) - P_{s,d} \right|. \tag{17}$$

Thus, the control tendency can be further written as

$$c_s(t) = \arg \min_{c_s \in \{c_{\min}, c_{\max}\}} \left| k_s y_{cf} \dot{y}_{cf} + c_s(t) \dot{y}_{cf}^2 - P_{s,d} \right|. \tag{18}$$

For the isolation objective considered here, the natural reference is $P_{s,d} = 0$. In this sense, the damping coefficient is selected so that the net power of the secondary suspension approaches the zero-power reference, thereby weakening vibration transmission through the secondary suspension.

Therefore, the main effect of ADD is not to directly regulate the carbody kinetic energy. Instead, ADD tends to reduce the power transmitted through the secondary suspension by making the secondary-suspension power approach the zero-power reference. The reduction in carbody acceleration is a consequence of this isolation-oriented mechanism.

For the PDD control, the control law is

$$c_s(t) = \begin{cases} c_{\max}, & \text{if } k_s y_{cf} \dot{y}_{cf} + c_{\max} \dot{y}_{cf}^2 \le 0, \\ c_{\min}, & \text{if } k_s y_{cf} \dot{y}_{cf} + c_{\min} \dot{y}_{cf}^2 > 0, \\ -\dfrac{k_s y_{cf}}{\dot{y}_{cf}}, & \text{otherwise.} \end{cases} \tag{19}$$

PDD can be regarded as a continuous realization of the same objective represented by ADD. Taking the desired secondary-suspension input power as $P_{s,d} = 0$, PDD can be further written as:

$$c_s(t) = \arg \min_{c_s \in [c_{\min}, c_{\max}]} \left| k_s y_{cf} \dot{y}_{cf} + c_s(t) \dot{y}_{cf}^2 \right|. \tag{20}$$

Compared with the discrete ADD logic, PDD provides a continuous realization of the same isolation-oriented objective. This continuous regulation is feasible only when the damper can be adjusted continuously within its admissible damping range.

The SH-ADD control strategy is given by

$$c_s(t) = \begin{cases} c_{\text{ADD}}, & \text{if } \ddot{y}_c^2 - a^2 \dot{y}_c^2 > 0, \\ c_{\text{SH}}, & \text{otherwise.} \end{cases} \tag{21}$$

where a is the frequency-selector parameter of SH-ADD. The complementarity between SH and ADD essentially reflects a coordinated switching between two distinct control objectives. When the kinetic energy of the carbody is high, priority should be given to regulating it. When the carbody acceleration becomes dominant, the priority shifts to reducing the transmitted suspension force. In this expression, $a^2 \dot{y}_c^2$ is directly related to the kinetic energy level of the carbody, whereas $\ddot{y}_c^2$ reflects the strength of the carbody acceleration. From this viewpoint, SH-ADD can be regarded as a switching realization of two coordinated objectives: regulating the carbody kinetic energy and isolating the carbody from the suspension input. However, this switching mechanism is still discontinuous, and its acceleration-based judgement may lead to force fluctuation when the measured signal or the response bandwidth of the actuator is not satisfactory (Guo & Wang, 2019).

In summary, SH regulates the carbody kinetic energy through the suspension power P_c. Since $\dot{H}_c = P_c$, increasing the damping when the suspension performs negative work on the carbody and reducing the damping when it would input positive power helps decrease the carbody kinetic energy and improve the lateral vibration performance. In contrast, ADD and PDD regulate the net suspension power P_s toward zero, thereby weakening the vibration transmitted from the bogie frame to the carbody through the secondary suspension. Therefore, semi-active control involves coordination between carbody kinetic-energy regulation and suspension-input isolation.

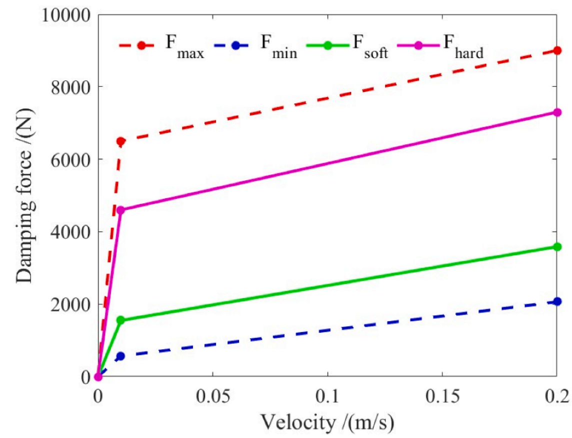

Fig. 4. Damping force characteristics.

3.3. Numerical simulation and analysis

To analyze the performance of classical control strategies presented above, a frequency-sweep simulation is carried out. The lateral track-displacement excitation is set to 4 mm, and the excitation frequency ranges from 0.1 to 10 Hz with a step size of 0.1 Hz.

To compare the vibration response of different control strategies, a transmissibility of carbody lateral acceleration (Savaresi & Spelta, 2007) relative to lateral track displacement is defined as

$$\hat{F}_c(f) = \sqrt{\frac{\sum_i \ddot{y}_{c,i}^2}{\sum_i y_{r,i}^2}}. \tag{22}$$

Here, f is the excitation frequency, $\ddot{y}_c$ is the carbody lateral acceleration, and y_r is the lateral track-displacement excitation. The transmissibility is used to evaluate the effectiveness of each control strategy over the frequency range. Additionally, the following maximum carbody kinetic energy index is introduced:

$$H_{c,\max}(f) = \frac{1}{2} m_c \dot{y}_{c,\max}^2. \tag{23}$$

Here, m_c denotes the carbody mass, and $\dot{y}_{c,\max}$ denotes the maximum carbody lateral velocity.

The damper is modeled using a Maxwell model, and the series stiffness is set to 20×10^6 N/m. The static force characteristic of the damper is shown in Fig. 4, where $F_{\max}$ and $F_{\min}$ denote the maximum and minimum damping forces of the adjustable damper, while F_{soft} and F_{hard} represent the passive soft-damping and passive hard-damping cases, respectively. Since a semi-active actuator cannot change its damping state instantaneously, a first-order inertial element $G(s)$ is introduced to represent the response bandwidth:

$$G(s) = \frac{1}{\frac{1}{b}s + 1}. \tag{24}$$

Here, b is the response bandwidth, which is set to 25π.

The resulting frequency response curves are shown in Fig. 5(a). When the excitation frequency approaches the lateral natural frequency of the carbody, the carbody acceleration response increases sharply. Under this condition, SH and SH-ADD achieve better vibration performance than ADD and the passive soft-damping suspension. Fig. 5(b) shows the kinetic energy of the carbody across different frequencies. Near resonance, a considerable amount of vibration energy has already accumulated in the carbody. Accordingly, the key control task is to enhance the negative power performed by the suspension on the carbody, or to reduce the positive power input transmitted through the damping port, so that the carbody kinetic energy can decrease more effectively. This observation is consistent with the energy-flow analysis presented in Section 3.2.

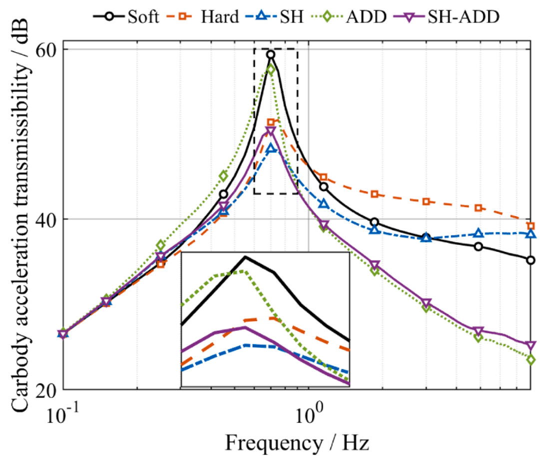

(a) Carbody acceleration response curves under different strategies.

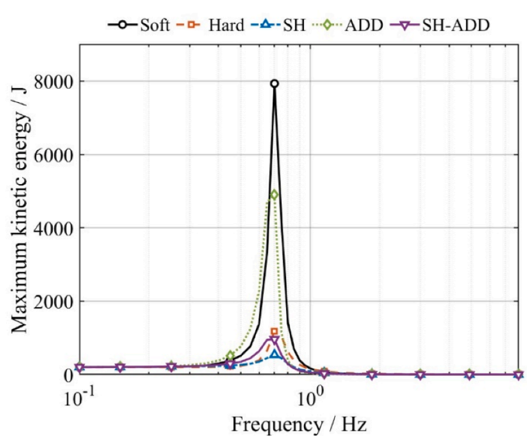

(b) Carbody kinetic energy frequency response curve.

Fig. 5. Carbody acceleration transmissibility and kinetic energy under different control strategies.

At higher frequencies, the response is increasingly influenced by forced vibration. In this range, ADD and SH-ADD provide better vibration isolation performance, while SH and the passive hard-damping lead to larger carbody acceleration. Dissipating the kinetic energy already stored in the carbody becomes less effective. Instead, adjusting the damping to isolate the carbody from the bogie-frame vibration works better, because it more directly reduces carbody acceleration. Therefore, when forced vibration dominates, isolation-oriented control strategies have a clear advantage.

Overall, the frequency-sweep results show that the relative effectiveness of classical semi-active control laws changes with the dominant vibration mechanism. In the low frequency range, the strategy emphasizing carbody kinetic energy regulation is more effective. In the higher frequency range, where forced vibration becomes stronger, isolation of vibration transmitted from the bogie frame through the suspension becomes more important. This shift motivates the development of a control law that can coordinate these two effects. The proposed EFC strategy is introduced precisely on this basis.

4. Design of the proposed energy flow control strategy

Section 3 shows that the secondary lateral semi-active suspension has two complementary energy flow effects. The first effect is associated with the carbody kinetic energy. When the carbody kinetic energy is high, the controllable damping-power component at the carbody port should be regulated so that the suspension can absorb energy from the carbody or reduce the positive power input to the carbody. The second effect is associated with suspension-input isolation. When the vibration transmitted from the bogie frame becomes dominant, the resultant suspension force acting on the carbody should be reduced.

Based on these two effects, the proposed EFC strategy is constructed using two physical control branches: a carbody kinetic-energy regulation branch and a suspension-input isolation branch. An energy-flow allocation factor is then introduced to coordinate the two branches continuously according to the carbody energy state.

4.1. *Kinetic energy regulation branch*

The first branch is used to regulate the carbody kinetic energy. It is constructed from the carbody velocity at the suspension mounting point. This branch is motivated by previous studies on fractional order skyhook damping for railway vehicles, where fractional order shaping was shown to be useful for balancing vibration reduction and maximum suspension deflection (Zolotas & Goodall, 2018). Compared with an integer-order operator, a fractional order operator can continuously adjust both the magnitude and phase characteristics of a signal:

$$F_{KE} = -c_{sky} D^{\alpha}(\dot{y}_c). \tag{25}$$

where c_{sky} is the kinetic-energy regulation gain, and D^{α} is the fractional order differintegral operator. Under zero initial conditions, it is expressed in the Laplace domain as

$$\mathcal{L}\{D^{\alpha}x(t)\} = s^{\alpha}X(s). \tag{26}$$

When $\alpha > 0$, D^{α} represents a fractional derivative. When $\alpha < 0$, it represents a fractional integral. When $\alpha = 0$, it reduces to the identity operator and F_{KE} degenerates into the linear Sky-hook control.

Since the ideal fractional operator s^{α} cannot be implemented directly, the Oustaloup recursive filter is used here to obtain a rational approximation over a prescribed frequency band. If the approximation band is $[\omega_b\ ,\ \ \omega_h]$ and the approximation order is N, then

$$s^{\alpha} \approx \omega_h^{\alpha} \prod_{k=-N}^{N} \frac{s+\omega_k^*}{s+\omega_k}. \tag{27}$$

Here

$$\begin{aligned} \omega_k^* &= \omega_b \left(\frac{\omega_h}{\omega_b}\right)^{\frac{k+N+0.5-0.5\alpha}{2N+1}}, \\ \omega_k &= \omega_b \left(\frac{\omega_h}{\omega_b}\right)^{\frac{k+N+0.5+0.5\alpha}{2N+1}}. \end{aligned} \tag{28}$$

Here, $\omega_b = 0.01$ rad/s and $\omega_h = 100$ rad/s are chosen to cover the main dynamic frequency range of the suspension system, and $N = 3$ is selected as an engineering compromise between approximation accuracy and filter order.

4.2. *Suspension input isolation branch*

The second branch is used to reduce the vibration input transmitted from the bogie frame to the carbody through the secondary suspension. According to the carbody equation of motion, the secondary spring force is one of the main components of the suspension force acting on the carbody. In the ideal isolation case, the control force should partially compensate this spring-related force, so that the resultant suspension force transmitted to the carbody is reduced. Following the sign convention used in this study, the ideal suspension-input isolation branch is written as:

$$F_{ISO} = k_s y_{cf}. \tag{29}$$

Here, k_s is the gain of the suspension-input isolation branch. In the present study, it is set equal to the physical secondary lateral stiffness, namely $k_s = k_s c$. This choice makes the isolation branch correspond to compensation of the secondary spring-force component.

4.3. Energy flow control law

The two branches derived above represent two different control tendencies of the secondary semi-active suspension. The kinetic-energy regulation branch F_{KE} is used to regulate the suspension-carbody power interaction. The suspension-input isolation branch F_{ISO} is used to reduce the resultant force transmitted to the carbody. Therefore, the two branches are first combined into a unified desired force. A smooth energy flow allocation factor λ is introduced. It determines how much of the desired force is assigned to kinetic-energy regulation and how much is assigned to suspension-input isolation.

The desired control force is then written as

$$F_d = \lambda F_{KE} + (1-\lambda) F_{ISO}. \tag{30}$$

That is

$$F_d = -\lambda c_{sky} D^{\alpha}(\dot{y}_c) + (1-\lambda) k_{sc} y_{cf}. \tag{31}$$

Here, F_d is the desired control force of the secondary semi-active actuator. The weighting factor λ is defined as an energy flow allocation factor and is constructed from carbody velocity through a hyperbolic tangent function:

$$\lambda = \tanh\left[(\beta \dot{y}_c)^4\right]. \tag{32}$$

Here, β is the weighting coefficient. The term $\dot{y}_c^4$ is used as a nonlinear energy-state indicator constructed from the carbody velocity. When the carbody kinetic energy is relatively large, λ increases and the control law places greater emphasis on regulating carbody kinetic energy. When the carbody kinetic energy is relatively small, λ remains small and the control law mainly focuses on isolating the vibration transmitted from the bogie frame through the suspension. In this way, the proposed control law realizes a smooth and continuous allocation between these two control objectives.

The tanh function provides a smooth and bounded mapping from the kinetic-energy-related variable to the allocation factor. Since $(\beta \dot{y}_c)^4$ is non-negative, the allocation factor remains within $[0,1)$, which is suitable for distributing the weights between the suspension input isolation branch and the kinetic energy regulation branch. At $\dot{y}_c = 0$, the derivative of λ with respect to the carbody velocity is zero, which reduces frequent weight variations caused by measurement noise and small velocity fluctuations. Once the carbody velocity leaves this narrow region, the fourth-power term causes λ to increase rapidly, so that the kinetic energy regulation branch can respond promptly even at relatively small vibration velocities. This allocation is consistent with Fig. 5, where SH provides better vibration attenuation than ADD around the main resonance frequency. As the velocity further increases, λ smoothly approaches 1 without introducing the slope discontinuity associated with piecewise switching. Therefore, the tanh function is selected for its bounded range, low sensitivity near zero, rapid response, and smooth saturation.

4.4. Numerical simulation and analysis

To analyze the weighting coefficient β, numerical simulations were carried out using the same vehicle model and damper model as those in Section 3.3. The mean value of the weighting factor, λ_{mean}, was used to describe the average allocation of the two control branches at each excitation frequency:

$$\lambda_{mean}(f) = \frac{1}{n}\sum_{i=1}^{n} \lambda_i. \tag{33}$$

Here, n denotes the number of sampling points, and λ_i is the value of λ at the ith sampling point. A larger λ_{mean} indicates that the control action places more emphasis on carbody kinetic-energy regulation. A smaller value indicates that the control action is mainly assigned to suspension-input isolation.

Fig. 6 shows the influence of β on the weighting factor and the acceleration transmissibility. As β increases, λ_{mean} increases mainly below about 2 Hz, while it remains close to zero in the higher-frequency range. This indicates that the controller gives more weight to carbody kinetic-energy regulation in the carbody-dominated vibration range, but still keeps the suspension-input isolation branch dominant at higher frequencies. As shown in Fig. 6(b), the response decreases in the range of 0.2–0.7 Hz, because the increased kinetic-energy regulation helps reduce the modal response of the carbody. However, the response increases in the range of 0.7–2 Hz when β becomes large, indicating that excessive weight on the kinetic-energy regulation branch may weaken the isolation effect near the resonance region. Therefore, β should be selected as a tradeoff parameter. When $\beta = 0$, the control law degenerates into the isolation branch. With increasing β, the controller allocates the control priority between kinetic-energy regulation and suspension-input isolation.

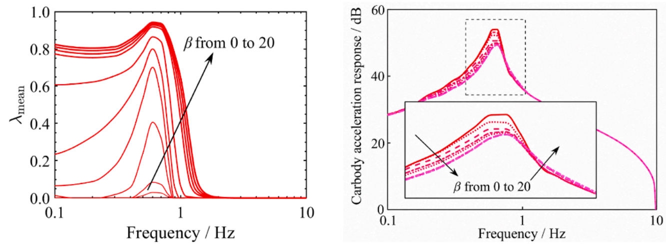

(a) Effect of β on λ. (b) Effect of β on transmissibility in EFC.

Fig. 6. Effect of β on the allocation factor λ and carbody acceleration transmissibility.

Fig. 7 shows the time domain and frequency domain responses under different control strategies. The frequency domain results show that EFC maintains good vibration control performance over 0.2–10 Hz. In the range of 0.2–0.7 Hz, its vibration reduction performance is close to that of SH and slightly better than that of SH-ADD. In the range of 1–5 Hz, its vibration-isolation performance is close to that of ADD and slightly better than that of SH-ADD. In the higher-frequency range of 5–10 Hz, EFC remains lower than or comparable to the best classical semi-active strategy. These results suggest that the weighting mechanism can coordinate the two control actions, namely carbody kinetic-energy regulation and suspension-input isolation, in a more balanced manner. The time-domain results further show that EFC produces a smoother response.

5. Full vehicle co-simulation with MR dampers

5.1. MR damper model

To evaluate the proposed EFC strategy in the full vehicle model, a mathematical model of the MR damper is established and incorporated into the co-simulation platform. Because the MR damper exhibits pronounced nonlinear hysteretic behavior, the Bouc–Wen model and its variants are widely used to describe its mechanical response. This study adopts a modified Bouc–Wen model to represent the damper behavior (Fu et al., 2024), and its structure is shown in Fig. 8.

The mathematical form of the model is given by

$$\begin{cases} \dot{z} = -\gamma|\dot{x}_m - \dot{x}_{c1}|\,|z|^{n-1}z - \xi(\dot{x}_m - \dot{x}_{c1})|z|^n + A(\dot{x}_m - \dot{x}_{c1}), \\ (c_0 + c_1)\dot{x}_{c1} = \alpha_{\mathrm{BW}} z + k_0(x_m - x_{c1}) + c_0\dot{x}_m, \\ F = c_1\dot{x}_{c1} + k_1 x_m + f\tanh(k_f x_m) + m_b\ddot{x}_m. \end{cases} \tag{34}$$

The nonlinear hysteresis of the damper itself is only one aspect of the actuator dynamics. In practice, there is also a dynamic lag between the control current and the actual damping force (Chen et al., 2026). Therefore, a transfer function is introduced to capture this characteristic.

5.2. MR damper model validation

To verify the MR damper model, tests were performed at a fixed amplitude of 10 mm and frequencies of 1 Hz and 2 Hz, with the input

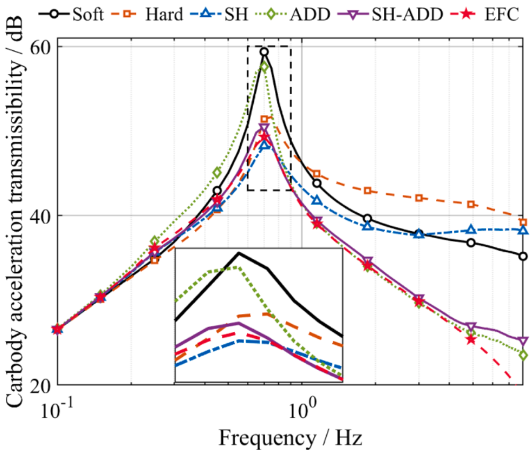

(a) Carbody acceleration response curves under different strategies.

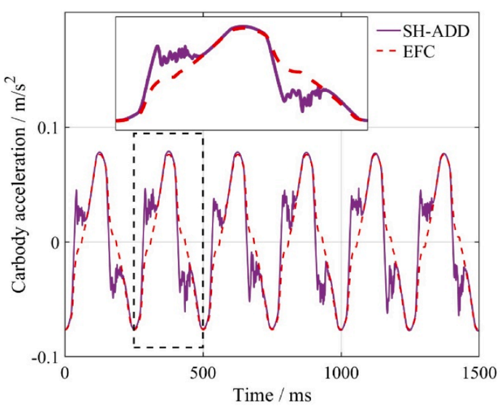

(b) Carbody acceleration time response curve.

Fig. 7. Time-domain and frequency-domain responses under different control strategies ($\beta = 20$).

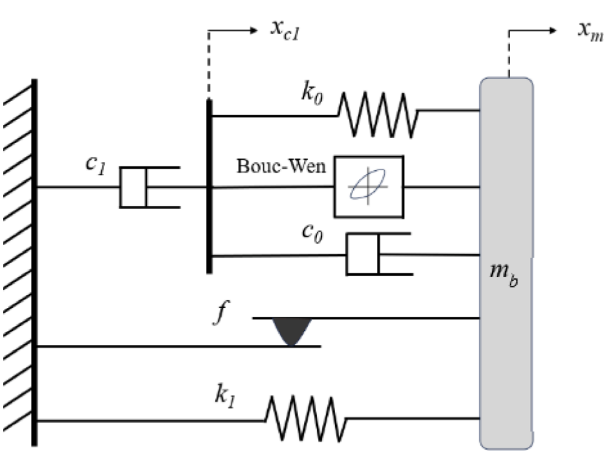

Fig. 8. Modified Bouc–Wen model of the MR damper.

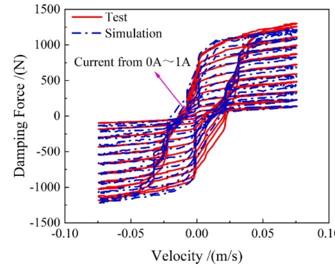

(a) 1 Hz, 10 mm.

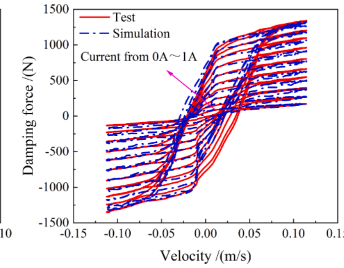

(b) 2 Hz, 10 mm.

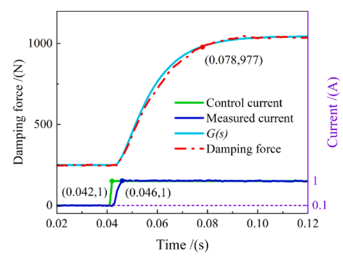

(c) Step-up current input.

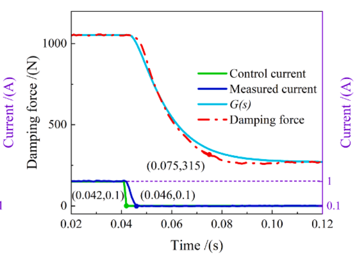

(d) Step-down current input.

Fig. 9. Comparison between experimental results and simulated results.

current swept from 0 to 1 A. Fig. 9(a) and (b) compare the measured and simulated force–velocity curves. The model captures both the hysteretic behavior and the variation in damping with current at both frequencies. Thus, the modified Bouc–Wen model represents the nonlinear characteristics of the tested MR damper with satisfactory accuracy.

The dynamic response was also examined using step-up and step-down current inputs. Fig. 9(c) and (d) show the measured current and the damping force response. The inertial delay during the current rise and fall is about 4 ms, indicating that the current drive loop of the MR damper is fast enough to reduce the delay between the control command current and the measured current. This is essential for real-time implementation of the semi-active control law on the HIL platform. At an excitation velocity of 0.1 m/s, the damping force response reaches about 90% of its steady state value within 35 ms. Therefore, a transfer function $G(s)$ is introduced to fit the lag between the damping force response and the control current, and the identified result is

$$G(s) = \frac{1 + T_z s}{(1 + T_{p1} s)(1 + T_{p2} s)(1 + T_{p3} s)} e^{-\tau s}. \tag{35}$$

Here, $T_{p1} = 0.003433745$, $T_{p2} = 0.0097444$, $T_{p3} = 0.0097903$, $T_z = 0.0079687$, and $\tau = 0.002$. The results show good agreement between the output of the transfer function and the measured damping force response, with a fitting accuracy exceeding 90%.

The modified Bouc-Wen model captures both the hysteretic force characteristics of the damper and the dynamic relationship between the control current and the damping force. Due to the limitation of the available test rig and prototype damper, the force level of the tested MR damper is lower than the force demand of the secondary lateral suspension in the full-vehicle model. Therefore, an equivalent force-scaling factor of five is used in the subsequent co-simulation and HIL analyses. The same scaling factor is applied to all control strategies and does not change the EFC control logic, the energy flow allocation law, or the current-command calculation procedure. The semi-active current range is 0–1 A, with the soft- and hard-damping states corresponding to 0.3 A and 0.7 A, respectively.

It should be noted that F_d is only the desired control force. Because the MR damper is a semi-active actuator, the desired force must satisfy the feasible force range. Therefore, the desired force is converted into a control current through an inverse damper model constructed from the experimentally measured force–velocity–current characteristics (Chen et al., 2026; Fu et al., 2024), as shown in Fig. 10(a).

It should be noted that if the desired damping force and the feasible damping force at the relative velocity have opposite directions, the command current is set to 0 A; otherwise, the following interpolation-based lookup procedure is applied, with the absolute values of force and velocity used as the lookup inputs for convenience. The inverse model is implemented using piecewise linear interpolation. For a given relative damper velocity v_d, two neighbouring measured velocity points, v_k and v_{k+1}, are first selected. At a fixed current level i_j, the damper force at

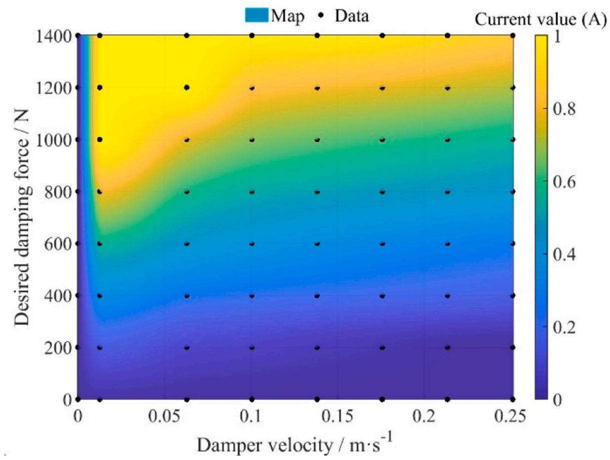

(a) Force-velocity-current inverse lookup map.

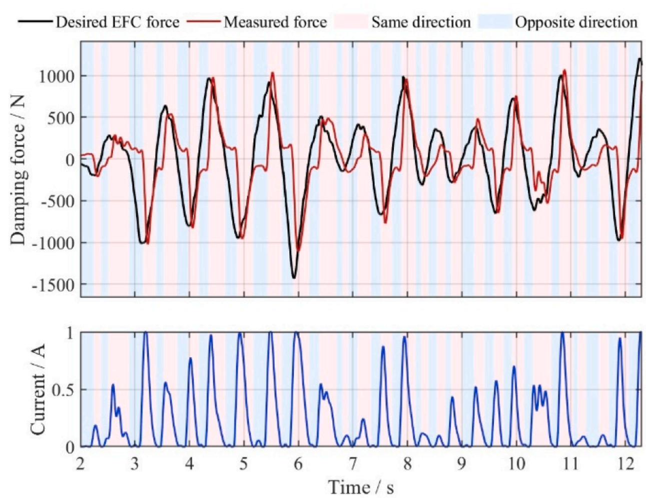

(b) Force realization result in a 10 s HIL test segment.

Fig. 10. Inverse model and force realization result of the MR damper.

v_d is obtained by linear interpolation:

$$\hat{F}(v_d, i_j) = F(v_k, i_j) + \frac{v_d - v_k}{v_{k+1} - v_k}\left[F(v_{k+1}, i_j) - F(v_k, i_j)\right]. \tag{36}$$

Here, $F(v_k, i_j)$ and $F(v_{k+1}, i_j)$ are the measured damper forces at the neighbouring velocity points, and $\hat{F}(v_d, i_j)$ is the interpolated force at the current relative velocity.

If the desired force F_d lies between the force values corresponding to two neighbouring current levels i_j and i_{j+1}, the preliminary command current is obtained by linear interpolation:

$$i^* = i_j + \frac{F_d - \hat{F}(v_d, i_j)}{\hat{F}(v_d, i_{j+1}) - \hat{F}(v_d, i_j)}\left(i_{j+1} - i_j\right). \tag{37}$$

Here, i^* denotes the preliminary command current obtained from the inverse lookup table before current saturation and low-velocity gain scaling. In this way, the measured force–velocity–current data are converted into a piecewise linear inverse mapping from (v_d, F_d) to the command current.

If the desired force is outside the feasible force range at the current relative velocity, i^* is limited to the nearest achievable current. To avoid unnecessary current fluctuations at very small damper velocities, an additional gain scaling is applied:

$$i = g_v(v_d)\,\mathrm{sat}_{[0,1]}\left(i^*\right). \tag{38}$$

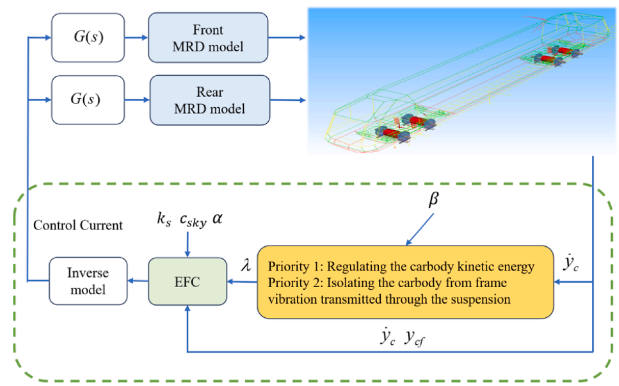

Fig. 11. Flowchart of the EFC suspension co-simulation model.

Here, i is the final command current, $\mathrm{sat}_{[0,1]}(\cdot)$ limits the current to the range of 0–1 A, and g_v increases linearly from 0 to 1 as the absolute relative velocity increases from 0 to 0.02 m/s.

To further illustrate the force realization process, a 10 s segment of the HIL test results in Section 6 is selected, as shown in Fig. 10(b). The controllable force generated by the MR damper does not always cover the desired force given by the EFC strategy. Therefore, the actual damper force may not completely follow the desired force at every instant. When the desired force lies within the feasible force range, the inverse model provides a suitable current command, and the measured damper force follows the desired force reasonably well. When the desired force cannot be realized because of the semi-active constraint, the command current is limited to the nearest feasible value.

5.3. Full-vehicle semi-active control simulation

5.3.1. Full-vehicle co-simulation platform with MR dampers

After validation, the MR damper model and the controller were implemented in MATLAB/Simulink and connected to the SIMPACK full vehicle multibody dynamics model through a co-simulation interface, forming the platform shown in Fig. 11. In this platform, the MR damper model serves as the semi-active actuator, and the inverse model converts the desired control force into a feasible control current. Compared with the simplified model, the full-vehicle model can describe the spatial vibration modes of the carbody, wheel–rail contact effects, and the dynamic coupling among the carbody, bogie frames, wheelsets, and traction motors. Therefore, this co-simulation platform is used to evaluate the performance of different suspension states and semi-active control strategies under full vehicle dynamic conditions. It also allows the sensitivity of the EFC parameters to be examined under a controlled periodic excitation.

5.3.2. Frequency-domain response and time delay effect under periodic excitation

Similar to the excitation setting used in the half-vehicle model analysis, both the lateral and vertical track excitations are defined as sinusoidal inputs with a wavelength of 10 m and an amplitude of 4 mm. The vehicle speed increases gradually from 0 to 140 km/h over a total simulation time of 1000 s. Therefore, the corresponding excitation frequency increases from 0 to approximately 3.89 Hz, covering the main frequency range of the carbody lateral vibration modes.

Fig. 12 shows the response of the full-vehicle co-simulation model. Since the excitation wavelength is fixed, the speed range of 30–50 km/h corresponds to an excitation frequency of approximately 0.83–1.39 Hz, which covers the main carbody swaying range identified from the full-vehicle model. For Fig. 12(a), the RMS carbody lateral acceleration is calculated using a 10 s moving window with a 1 s moving step. For Fig. 12(b), the angular-acceleration envelope is obtained from the local peaks of the absolute yaw, roll, and pitch angular-acceleration signals.

As shown in Fig. 12(a), the soft-damping and ADD suspensions exhibit a sharp response peak within the speed range of 30–50 km/h. This indicates that these two suspension states are less effective in suppressing the pronounced response when the periodic excitation approaches the carbody lateral modes. Hard damping limits the peak response, but its carbody acceleration remains relatively high over the subsequent speed range. In comparison, SH, SH-ADD, and EFC substantially suppress the peak. Among them, EFC maintains a relatively low response both in the main resonance region and at speeds above 60 km/h, indicating a better balance between suppressing the carbody modal response and limiting vibration transmission through the secondary suspension.

Fig. 12(b) presents the envelopes of the carbody yaw, roll, and pitch angular accelerations during the same speed sweep using soft-damping. In the interval corresponding to the main acceleration peak in Fig. 12(a), the yaw angular-acceleration envelope increases sharply and is substantially larger than the roll and pitch envelopes. This indicates that the pronounced carbody response is dominated by yaw motion. The roll envelope also increases in this interval, showing that carbody roll participates in the response, although its amplitude remains much lower than that of yaw. In contrast, the pitch angular-acceleration envelope remains relatively small and makes only a limited contribution to the main response peak.

After the main response region, the yaw angular-acceleration envelope decreases rapidly, while the yaw, roll, and pitch responses remain at relatively low levels over the subsequent speed range. These results directly show that the main peak in Fig. 12(a) is primarily associated with carbody yaw motion, accompanied by a smaller roll component.

In practical implementation, time delay is inevitably introduced by sensor measurement, signal processing, communication, and actuator response. Such delay may affect the closed-loop performance of semi-active control strategies, especially when the vibration frequency increases or when the control law contains switching logic. Based on the full-vehicle co-simulation model established in this section, the influence of additional control delay on the performance of the different control strategies is investigated.

The results in Fig. 12 identify the speed range in which the periodic excitation causes a pronounced carbody response. Accordingly, the same periodic excitation with a wavelength of 10 m and an amplitude of 4 mm is applied in the delay analysis. The simulation duration is 100 s. Two speed sweep ranges are considered: 30–50 km/h and 80–100 km/h. The first range covers the pronounced carbody swaying response, whereas the second range represents the response under a higher excitation frequency. These two cases are used to evaluate the delay sensitivity of the control strategies under different vibration conditions.

Fig. 13 compares the influence of additional control delay in the two representative speed ranges. Under the 10 m periodic excitation, 30–50 km/h corresponds to an excitation frequency of approximately 0.83–1.39 Hz and includes the main response peak shown in Fig. 12. The range of 80–100 km/h corresponds to approximately 2.22–2.78 Hz, where the response is more strongly affected by forced vibration transmitted through the secondary suspension. The influence of delay differs among the semi-active strategies. In particular, ADD exhibits a non-monotonic variation in the 30–50 km/h range, whereas the RMS responses of SH, SH-ADD, and EFC generally increase as the delay increases. Therefore, the delay limit of EFC is evaluated separately from the response trends of the other strategies.

In the 30–50 km/h range, the soft-damping suspension maintains a high RMS acceleration level, indicating that low damping is insufficient to suppress the pronounced carbody swaying response. The hard-damping suspension substantially reduces this response and therefore provides a more appropriate passive reference in this range. SH, SH-ADD, and EFC give lower RMS acceleration than the two passive suspensions when the delay is small. As the delay increases, the RMS response of EFC gradually rises. When the additional delay is not greater

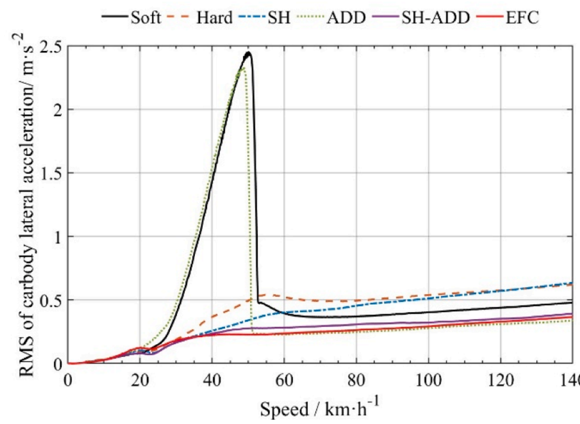

(a) RMS of carbody lateral acceleration.

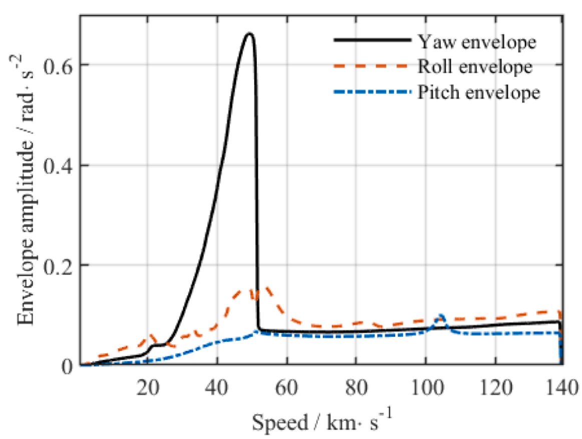

(b) Envelopes of carbody yaw, roll, and pitch angular accelerations.

Fig. 12. Co-simulation results under 10 m wavelength track excitation.

than approximately 60 ms, EFC still gives a lower RMS acceleration than both the soft-damping and hard-damping suspensions. Beyond this value, its advantage over the hard-damping suspension is no longer maintained.

In the 80–100 km/h range, the excitation frequency increases to approximately 2.22–2.78 Hz, and the EFC response becomes more sensitive to delay. EFC gives a lower RMS acceleration than both passive suspensions when the additional delay is not greater than approximately 30 ms. When the delay exceeds this value, the EFC response becomes higher than that of the better passive suspension, indicating that its control advantage is progressively weakened. SH also shows pronounced delay sensitivity in this frequency range, while ADD and SH-ADD exhibit different non-monotonic response trends because the delay changes the phase relationships used by their control laws.

5.3.3. Parameter sensitivity and selection of the EFC strategy

The dynamic behavior of metro vehicles varies significantly with wheel–rail conditions and speeds. This section focuses on the robustness of EFC parameters under different wheel profiles. The rail profile is CHN60, and two wheel profiles are considered: standard LM and worn LM. When matched with CHN60, their nominal equivalent conicities are 0.1 and 0.39, respectively. Speeds are 80 km/h and 100 km/h. The weighting coefficient β is set to 20, as analyzed in Section 4.4. The isolation-branch gain is fixed as $k_{sc} = k_s$, where k_s is the secondary lateral stiffness listed in Table 1. This section mainly examines the influence of the gain coefficient c_{sky} and the fractional order α. The range of c_{sky} is $[2, 30] \times 10^4$, with a step of 2×10^4, while α varies from -0.4 to 0.6 with a step of 0.1.

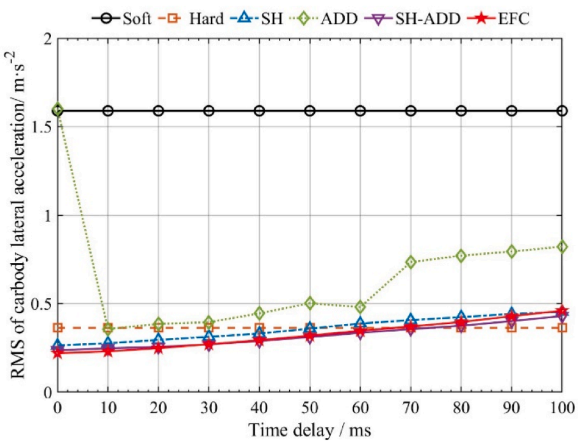

(a) 30–50 km/h.

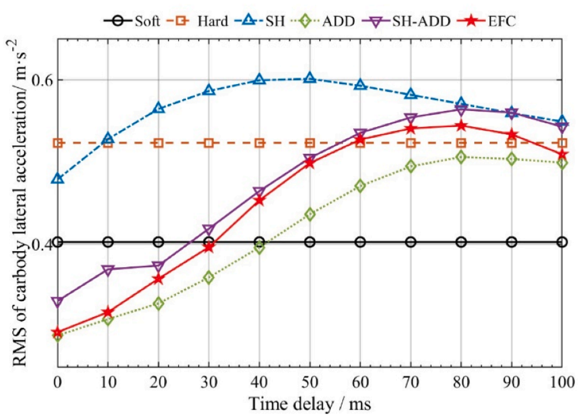

(b) 80–100 km/h.

Fig. 13. Time delay influence on different control strategies.

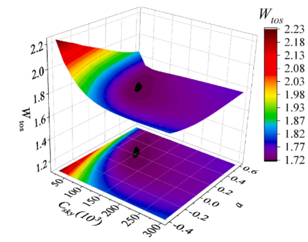

(a) W_{tos}.

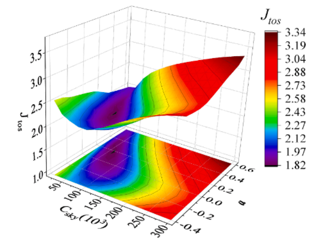

(b) J_{tos}.

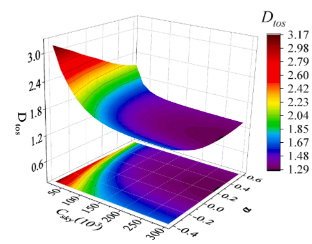

(c) D_{tos}.

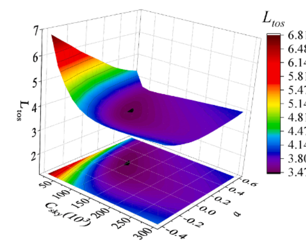

(d) L_{tos}.

Fig. 14. Influence of control parameter variation on the evaluation indices under the worn LM wheel condition.

To evaluate how the control parameters affect the full vehicle dynamic performance, three ratios are defined at a running speed of i km/h: the ratios of the lateral Sperling index, the RMS value of carbody jerk, and the RMS value of suspension dynamic deflection under the EFC suspension to those under the soft-damping suspension. These are denoted by W^i_{tos}, J^i_{tos}, and D^i_{tos}, respectively. A comprehensive index L_{tos} is further introduced to assess the overall control performance. This index takes Sperling index as the primary objective while also considering suspension displacement and carbody jerk. The weights are chosen empirically for parameter selection in this study and are not intended as the optimal choice for other vehicles or engineering objectives.

$$\begin{cases} W_{tos} = W^{80}_{tos} + W^{100}_{tos}, \\ J_{tos} = J^{80}_{tos} + J^{100}_{tos}, \\ D_{tos} = D^{80}_{tos} + D^{100}_{tos}, \\ L_{tos} = W_{tos} + 0.1 J_{tos} + 0.1 D_{tos}. \end{cases} \tag{39}$$

Figs. 14 and 15 show the response surfaces of the evaluation indices with respect to c_{sky} and α under different wheel profiles. All indices have broad regions in the parameter space, not a single isolated optimum. Under the worn LM condition, the optimal parameter combinations for W_{tos}, J_{tos}, D_{tos}, and L_{tos} are $(1.0 \times 10^5, 0.2)$, $(6 \times 10^4, 0.2)$, $(3 \times 10^5, 0.3)$, and $(1.0 \times 10^5, 0.2)$, respectively. Under the LM condition, the corresponding best parameter combinations within the tested parameter grid are $(1.4 \times 10^5, 0.3)$, $(6 \times 10^4, 0.1)$, $(3 \times 10^5, 0.2)$, and $(1.2 \times 10^5, 0.2)$. These results indicate that different performance indices do not favor exactly the same parameter values. A larger c_{sky} is more beneficial for reducing suspension displacement, whereas a relatively smaller c_{sky} is more favorable for reducing carbody jerk. The favorable range of α is relatively concentrated, mainly between 0.1 and 0.3.

There is a clear compromise between D_{tos} and J_{tos} in the choice of c_{sky}. Under the LM condition, for example, when $\alpha = 0.2$, increasing c_{sky} from 2×10^5 to 3×10^5 reduces D_{tos} from 1.259 to 1.232, so the suspension displacement improves to some extent. At the same time, however, J_{tos} rises from 2.688 to 3.079, which is clearly worse than the minimum value of 1.757 in the tested parameter grid. A similar trend is also observed under the worn LM condition. Therefore, it is not appropriate to optimize the controller using only a single performance index. Instead, the control parameters should be selected by balancing Sperling index, suspension displacement, and carbody jerk. The comprehensive index L_{tos} is introduced precisely to reflect this need for multi-index coordination.

The sensitivity analysis shows that the comprehensive index L_{tos} has a relatively broad favorable region. For each wheel profile, when c_{sky} varies within $\pm 4 \times 10^4$ N s/m around the corresponding L_{tos}-optimal value and α varies within ± 0.1 around its corresponding optimum, the relative variation in L_{tos} remains below 3%. Moreover, when the final selected parameter set is applied to either wheel profile, the increase in L_{tos} relative to the profile-specific minimum remains below 3%.

The L_{tos} response surfaces show a favorable region around $\alpha = 0.2$ and $c_{\mathrm{sky}} = (1.0\text{–}1.2) \times 10^5$ N s/m. Considering the Sperling index, suspension displacement, carbody jerk, and adaptability under different wheel–rail matching conditions, $c_{\mathrm{sky}} = 1.1 \times 10^5$ N s/m and $\alpha = 0.2$ are selected for the subsequent HIL tests. This parameter set lies within the favorable region of the comprehensive index L_{tos} and maintains stable control performance across different wheel profiles and speeds, without requiring complex multiobjective optimization for parameter tuning.

6. Full-vehicle hardware-in-the-loop experimental verification

6.1. Hardware-in-the-loop test platform

To further verify the effectiveness of the proposed EFC strategy under real actuator conditions, a HIL test platform was constructed. Fig. 16 shows the principle of the HIL setup. In the figure, the blue lines indicate signal transmission paths, the red boxes mark the physical hardware, and the green boxes give the names of the corresponding hardware units. Before the test, the metro vehicle model established in SIMPACK was imported into Concurrent Simulator(1). The control programs for the

Table 2
Evaluation indices under the worn LM wheel.

Control strategy	Lateral Sperling index		RMS of displacement / mm		RMS of jerk / $\mathrm{m\,s^{-3}}$	
	80 km/h	100 km/h	80 km/h	100 km/h	80 km/h	100 km/h
Soft	2.33	2.42	5.78	6.32	3.41	4.13
Hard	2.61(−12.0%)	2.70(−11.6%)	4.47(22.7%)	4.68(25.9%)	5.41(−58.7%)	6.47(−56.7%)
SH	2.24(3.9%)	2.32(4.1%)	4.31(25.4%)	4.27(32.4%)	4.65(−36.4%)	5.21(−26.2%)
ADD	2.11(9.4%)	2.20(9.1%)	6.74(−16.6%)	6.97(−10.3%)	5.91(−73.3%)	6.50(−57.4%)
SH-ADD	2.12(9.0%)	2.16(10.7%)	4.61(20.2%)	4.58(27.5%)	5.52(−61.9%)	6.01(−45.5%)
EFC	2.06(11.6%)	2.13(12.0%)	4.57(20.9%)	4.59(27.4%)	4.44(−30.2%)	4.91(−18.9%)

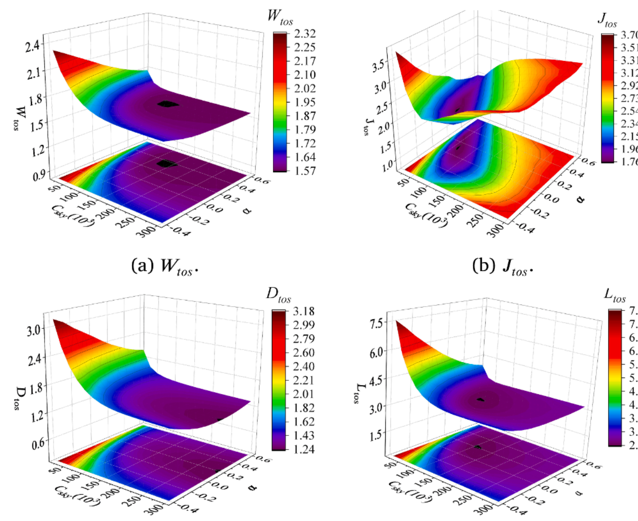

(a) W_{tos}. (b) J_{tos}. (c) D_{tos}. (d) L_{tos}.

Fig. 15. Influence of control-parameter variation on the evaluation indices under the LM wheel condition.

different strategies were implemented in LINKS Simulator(3), and the current driving program was loaded into Current Control(6).

During the test, the vehicle model ran in real time in Concurrent Simulator (1), while the control algorithm was executed in LINKS Simulator (3). The two modules exchanged vehicle vibration signals and damping force information through UDP communication. The displacement servo system (4) drove the servo motor (5) according to the real-time relative suspension displacement, and the motor then applied mechanical excitation to the MR damper (7). The current controller (6) generated the driving current according to the selected control strategy, and the force sensor (8) measured the damping force in real time and fed it back to LINKS Simulator. The online simulation step size was 1 ms, and the sampling resolution was 16-bit AD, which was sufficient for operation in real time. To make the test closer to an actual engineering environment, measured idle noise was added to the vehicle vibration signals to simulate the measurement noise of sensor (2). To reduce the influence of measurement noise, differentiation, and discrete switching on the control strategies, a second-order Butterworth low-pass filter with a cutoff frequency of 30 Hz was applied at the signal acquisition stage.

6.2. Analysis of evaluation results

Tables 2 and 3 summarize the lateral Sperling index, the RMS secondary suspension displacement, and the RMS carbody jerk for different suspension states at 80 km/h and 100 km/h, under the worn LM and LM wheel, respectively. No single strategy is optimal for all three indices. For lateral Sperling index, EFC yields the best result under all four cases. For carbody jerk, the soft-damping suspension performs best, whereas EFC gives the lowest jerk among the semi-active strategies. In terms of suspension displacement, SH gives the smallest value in all four cases, and EFC remains close to the second best.

Looking first at the lateral Sperling index, EFC achieves the lowest value in all four cases. Under the worn LM, the values are 2.06 and 2.13 at 80 km/h and 100 km/h, respectively. Under the LM, they are 1.84 and 1.94. Compared with the soft-damping suspension, EFC improves the Sperling index by 11.6%–12.0% under worn LM and by 18.1%–19.7% under LM. Even relative to SH-ADD, EFC gives a further improvement of 1.4%–3.5%. Therefore, the Sperling-index improvement of EFC over SH-ADD is moderate but consistent, which is expected because SH-ADD already provides strong semi-active control performance by coordinating SH and ADD actions. The advantage of EFC is not only reflected in the Sperling index, but also in its lower jerk and competitive suspension displacement. On the unfavorable side, the hard-damping gives the worst Sperling index under the worn LM, with Sperling indices of 2.61 and 2.70, whereas the soft-damping suspension performs worst under the LM, with values of 2.29 and 2.37. This again highlights the limitation of fixed passive damping, namely that a single damping setting cannot maintain satisfactory Sperling index under different wheel–rail matching conditions.

The suspension displacement results show a different tendency. SH gives the smallest RMS displacement in all four cases, with values of 4.31 mm and 4.27 mm under worn LM, and 4.19 mm and 4.47 mm under LM. The corresponding values of EFC are only 6.0%–9.4% higher than those of SH, which places EFC at or near the second-best. Compared with the soft-damping, EFC still reduces suspension displacement by 20.9%–27.4% under worn LM and by 28.6%–43.4% under LM. Therefore, the ride-quality improvement from EFC does not come at the cost of a large increase in suspension displacement. At the opposite end, ADD produces the largest or near-largest suspension displacement, reaching 6.74–8.01 mm, followed by the soft-damping. This suggests that when the control action is biased too strongly toward input isolation alone, larger elastic deformation is retained in the suspension and more energy remains stored in the elastic elements.

The jerk results are also instructive. The soft-damping gives the lowest jerk in all four cases, with values of 3.41 and 4.13 under worn LM, and 3.16 and 3.93 under LM. This is not contradictory, because the smaller damping level of the soft-damping also weakens the transmission of high-frequency force, thereby naturally reducing jerk. The trade-off is that its Sperling index and suspension-displacement performance are insufficient. Among the semi-active strategies, EFC consistently gives the lowest jerk, with values of 4.44 and 4.91 under worn LM, and 4.32 and 4.61 under LM. Compared with SH-ADD, EFC further reduces jerk by 12.0%–19.6% under all four operating conditions. Thus, EFC gives the lowest Sperling index among the tested strategies while keeping jerk below that of ADD and SH-ADD. This result is consistent with the expectation that smoother control can reduce the additional high-frequency chattering introduced by discrete switching and on-off control laws. ADD gives the largest jerk in all four cases, reaching 5.91–6.55.

Fig. 17 provides a more intuitive comparison of the overall control performance. EFC is not optimal for every single index individually; its advantage is that it improves Sperling index while keeping jerk and suspension displacement within a competitive range. Its main advantage

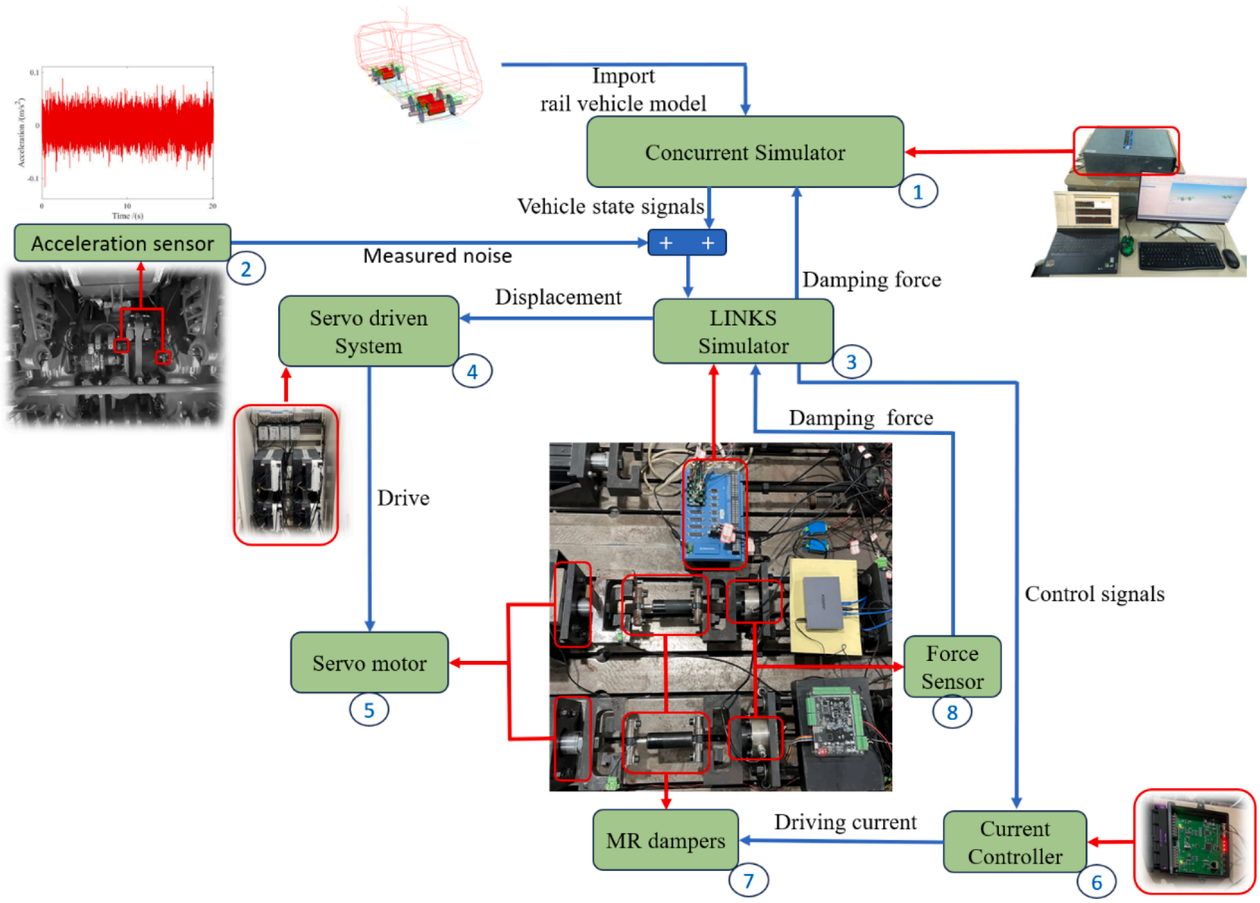

Fig. 16. Schematic of the hardware-in-the-loop test platform.

Table 3
Evaluation indices under the LM wheel.

Control strategy	Lateral Sperling index		RMS of displacement / mm		RMS of jerk / m s^{-3}	
	80 km/h	100 km/h	80 km/h	100 km/h	80 km/h	100 km/h
Soft	2.29	2.37	7.92	6.85	3.16	3.93
Hard	2.07(9.6%)	2.30(3.0%)	5.22(34.1%)	5.31(22.5%)	4.27(−35.1%)	4.62(−17.6%)
SH	1.89(17.5%)	2.04(13.9%)	4.19(47.1%)	4.47(34.7%)	4.62(−46.2%)	4.73(−20.4%)
ADD	2.18(4.8%)	2.27(4.2%)	7.59(4.2%)	8.01(−16.9%)	6.04(−91.1%)	6.55(−66.7%)
SH-ADD	1.88(17.9%)	2.01(15.2%)	4.58(42.2%)	5.01(26.9%)	4.91(−55.4%)	5.27(−34.1%)
EFC	1.84(19.7%)	1.94(18.1%)	4.48(43.4%)	4.89(28.6%)	4.32(−36.7%)	4.61(−17.3%)

is that it achieves a more balanced coordination among the three key indices. EFC does not reach the minimum jerk of the soft-damping, but among all semi-active strategies it performs best in this aspect. A similar pattern appears in suspension displacement: EFC is slightly inferior to the best-performing SH strategy, yet it does not improve ride quality at the expense of a marked deterioration in displacement performance. SH-ADD also gives strong semi-active control performance, but this is accompanied by a higher jerk penalty. Compared with the other semi-active strategies, EFC provides the best lateral ride-quality index and the lowest RMS jerk under all four operating cases, while keeping the suspension displacement close to the second-best level. For railway semi-active suspension, this type of balanced performance is more meaningful in engineering practice than the minimization of a single index alone.

Table 4 shows the maximum track shift force under different suspension states. When the speed increases from 80 km/h to 100 km/h, the maximum track shift force increases for all suspension states. The hard-damping suspension gives the smallest value at both speeds. The four semi-active control strategies show comparable maximum track shift force, but their values are slightly higher than those of the hard-damping suspension. Therefore, the semi-active suspension improves the carbody lateral dynamic performance, with only a limited increase in the maximum track shift force.

Table 4
Maximum track shift force / kN under different control strategies and operating speeds.

Speed	Soft	Hard	SH	ADD	SH-ADD	EFC
80 km/h	13.21	13.08	14.44	13.67	14.21	14.38
100 km/h	18.36	17.15	19.03	19.71	19.38	19.59

6.3. Time-domain and frequency-domain analysis

The time-domain responses in Fig. 18(a) show that EFC effectively reduces the lateral acceleration of the carbody, whereas the response under EFC is visibly smoother and contains fewer local spikes and less high-frequency chattering. This is especially clear in the enlarged view, where the EFC curve is more continuous than those of the other semi-active

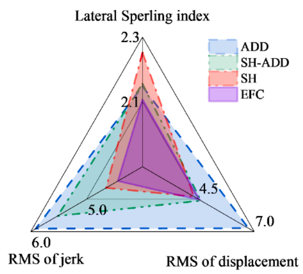

(a) 80 km/h under worn LM.

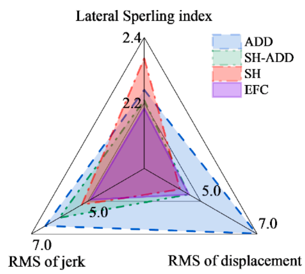

(b) 100 km/h under worn LM.

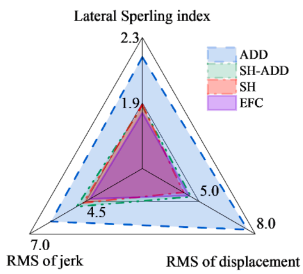

(c) 80 km/h under LM.

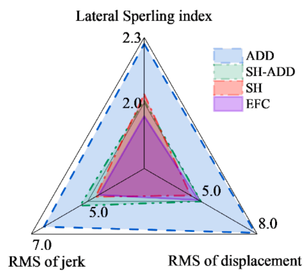

(d) 100 km/h under LM.

Fig. 17. Comparison of evaluation indices under different control strategies, wheel profiles, and operating speeds.

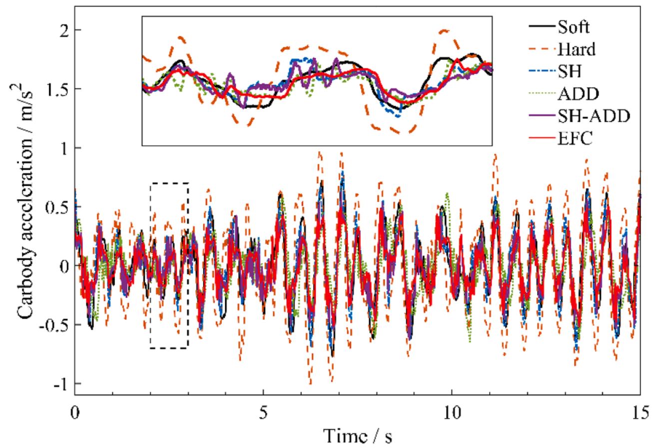

(a) Time histories of front-end carbody lateral acceleration under different suspension states.

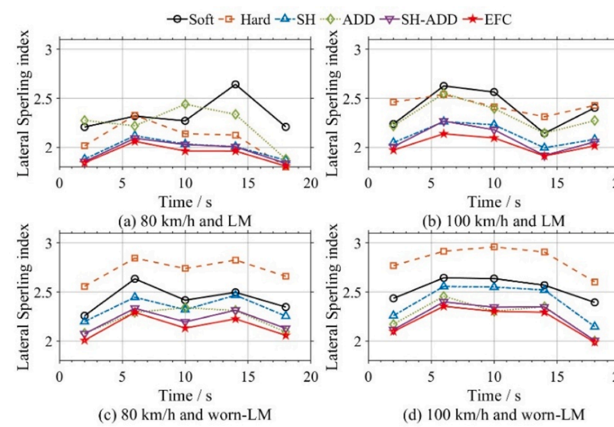

(b) Lateral Sperling index calculated using a 4 s moving window.

Fig. 18. Time-domain responses under different suspension states.

strategies. Even with actuator response lag and measurement noise, the continuous weighting mechanism still reduces the chattering that often appears in switching control.

Fig. 18(b) shows the time histories of the lateral Sperling index calculated using a 4 s moving window over a 20 s test period. Compared with the overall values listed in Tables 2 and 3, this time-varying index provides a clearer view of the local ride-quality variation during the test. The soft-damping and hard-damping suspensions show noticeable local deterioration in several time windows. This is especially clear under the 100 km/h worn-LM condition, where the hard-damping suspension exceeds the excellent-level threshold in several moving windows. This indicates that a fixed damping setting cannot maintain consistent ride quality under different wheel profiles and operating speeds.

Under the LM wheel profile, EFC, SH-ADD, and SH all reduce the lateral Sperling index effectively. In the 80 km/h LM case, the overall vibration level is relatively low, but the soft-damping suspension still shows a local peak around the middle of the test period. EFC keeps a lower value throughout the test. In the 100 km/h LM case, both the soft-damping and hard-damping suspensions exceed the excellent-level threshold in some windows, whereas EFC remains close to 2.0 and gives the lowest or near-lowest value over the whole period. Under the worn-LM wheel profile, the lateral vibration becomes stronger and the advantage of semi-active control is more evident. The soft- and hard-damping suspensions show higher time-varying Sperling indices, especially at 100 km/h. In contrast, EFC maintains a relatively low Sperling index throughout the test and remains lower than, or close to, the best result among the compared strategies. This demonstrates that EFC not only reduces the overall ride-quality index, but also suppresses local deterioration of ride quality within short time windows.

Therefore, Fig. 18(b) confirms the time-domain consistency of the proposed EFC strategy. The benefit of EFC is not limited to the reduction of the overall statistical index. It also provides a more stable time-varying ride-quality performance under different wheel profiles and speeds, which is important for metro vehicles operating under variable wheel–rail contact conditions.

Modal analysis of the SIMPACK vehicle model shows that 0.85 Hz and 1.42 Hz correspond to the carbody yaw mode and the upper sway mode, respectively. Previous studies have shown that when the bogie hunting frequency approaches the natural frequency of carbody lateral modes, coupled vibration is more likely to occur and the lateral ride quality can deteriorate (Chen et al., 2018). Fig. 19 shows that the locations of the main spectral peaks and the distribution of response energy vary with wheel profile and operating speed. Under the LM condition, the response energy is concentrated mainly near 1 Hz and is more closely associated with low-frequency carbody modal participation. Under the worn LM condition, the dominant peak shifts toward about 2 Hz, and the response above 2 Hz becomes more pronounced as speed increases. This spectral change is consistent with an increased contribution from vibration transmitted through the suspension and from coupled response components.

Under the LM wheel profile, the dominant carbody vibration is mainly concentrated around 1 Hz. This frequency is close to the low-frequency carbody modes identified by modal analysis. Under this condition, SH, SH-ADD, and EFC all reduce the dominant modal response effectively, whereas ADD is less effective around this range. This is consistent with the energy flow analysis in Section 3.3: when the carbody modal response is dominant and the carbody kinetic energy becomes large, control action that regulates the carbody-side power interaction is more effective.

Under the worn LM wheel profile, the dominant peak shifts toward about 2 Hz, and the response components above 2 Hz become more pronounced, especially at 100 km/h. This suggests that the response contains stronger forced-vibration and coupled components, rather than only a simple amplification of the low-frequency carbody mode. In this condition, the advantage of ADD becomes more visible in part of the higher-frequency range, because reducing the effective suspension input transmitted from the bogie frame is more important when forced

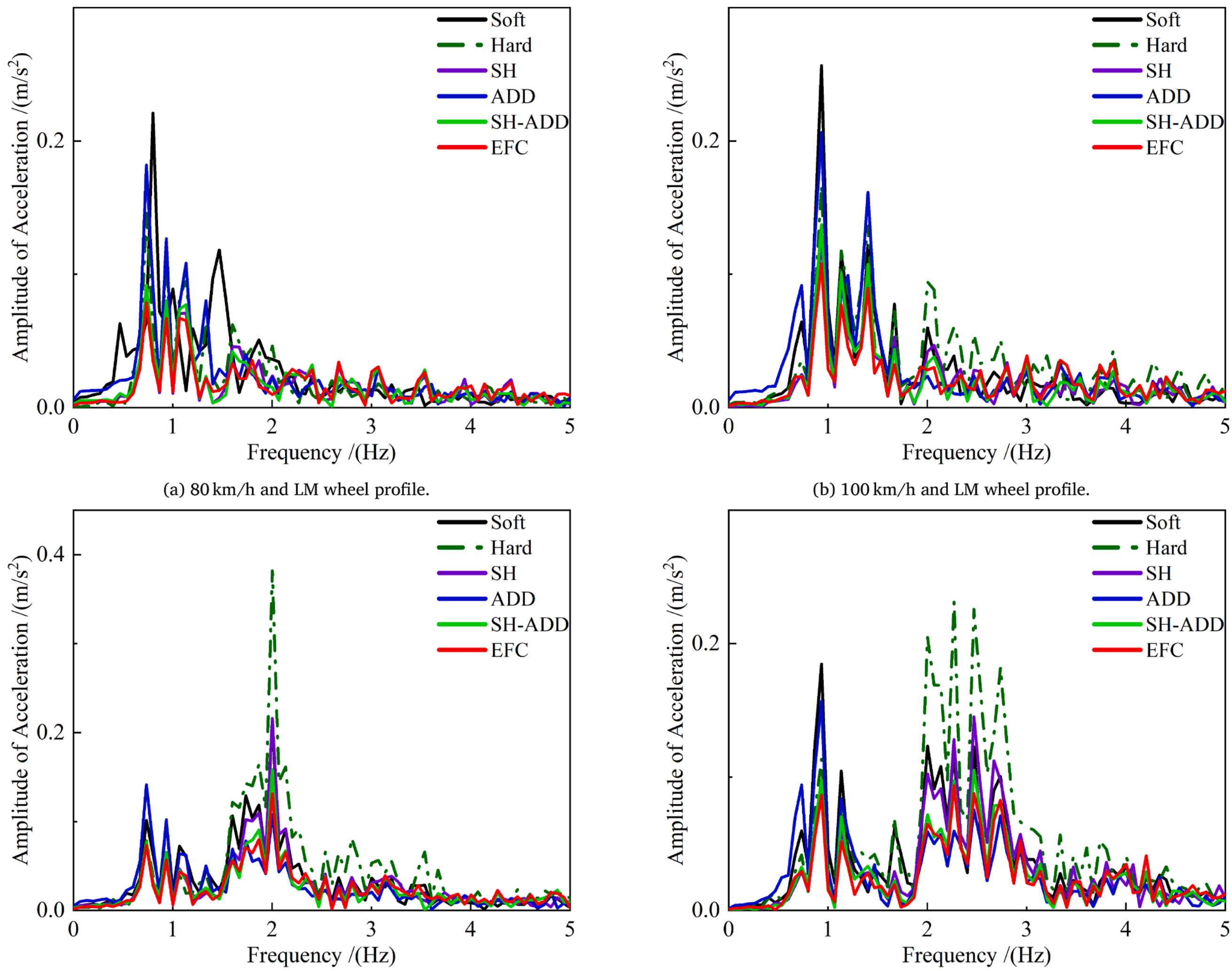

(a) 80 km/h and LM wheel profile.

(b) 100 km/h and LM wheel profile.

(c) 80 km/h and worn LM wheel profile.

(d) 100 km/h and worn LM wheel profile.

Fig. 19. Frequency spectra of carbody lateral vibration under different control strategies, wheel profiles, and operating speeds.

vibration becomes stronger. However, ADD alone cannot provide the best overall result, because it does not sufficiently reduce the lower-frequency modal component and may increase jerk.

EFC avoids these limitations by coordinating the two effects continuously according to the smooth kinetic-energy-based weighting function. As a result, the key advantage of EFC is not limited to one dominant vibration mechanism. It maintains a comparatively low response level in the low-frequency modal range, the higher frequency response range, and the intermediate coupled frequency region, which directly reflects the benefit of continuously coordinating carbody kinetic-energy regulation and isolation of vibration transmitted from the bogie frame through the suspension.

Due to the limitations of the test platform, very severe operating conditions with a Sperling index higher than 3.0 were difficult to reproduce in the HIL tests. The main constraints were the power limit of the electric cylinder and the allowable stroke of the MR damper. In addition, when high-frequency excitation above 10 Hz was applied, the response delay of the servo motor could cause instability of the bogie-side excitation loop. These factors should be considered in future experimental studies, especially when extending the HIL platform to more severe vibration conditions or higher excitation frequencies.

7. Conclusion and discussion

Based on the theoretical analysis, full vehicle co-simulation, and HIL tests, the proposed EFC strategy improves the overall lateral vibration performance of the metro vehicle under the combined conditions of wheel profiles (LM, equivalent conicity is 0.1; worn LM, equivalent conicity is 0.39) and operating speeds (80 km/h and 100 km/h). The main conclusions are as follows:

1. An energy-flow interpretation was developed for the secondary lateral semi-active suspension based on the power interaction between the carbody, secondary suspension, and bogie frame. The analysis shows that classical semi-active control laws mainly correspond to two physical effects: carbody kinetic energy regulation and isolating the carbody from bogie-frame vibration transmitted through the suspension. On this basis, EFC was developed to coordinate these two effects through a smooth weighting mechanism and a fractional order operator.
2. The full vehicle co-simulation results show that EFC has good parameter robustness. When the parameters vary within the specified neighborhood of the corresponding L_{tos}-minimum point, or when

the selected parameter set is transferred between the two wheel conditions, the degradation of the comprehensive index remains within 3%. The delay analysis shows that, in the 0.83–1.39 Hz and 2.22–2.78 Hz vibration ranges, the allowable additional control delay for EFC is approximately 60 ms and 30 ms, respectively, while its RMS carbody acceleration remains lower than those of both passive suspension states.

3. HIL tests show that EFC achieves the best lateral Sperling index under all investigated conditions. The soft-damping suspension gives the lowest jerk, while EFC gives the lowest jerk among the semi-active strategies. The SH gives the smallest suspension displacement, followed by EFC and SH-ADD. Compared with the soft-damping, EFC improves the Sperling index by 11.6%–19.7% and reduces suspension displacement by 20.9%–43.4%. Compared with SH-ADD, EFC improves the Sperling index by about 1.4%–3.5% and reduces carbody jerk by about 12.0%–19.6%. When the wheel profile changes from LM to worn LM, the dominant response shifts from around 1 Hz toward about 2 Hz, and the higher-frequency components become more pronounced at 100 km/h. By coordinating carbody kinetic-energy regulation and suspension-input isolation, EFC maintains good adaptability across the tested wheel profiles and speeds. All control strategies were successfully executed within each 1 ms real-time control step on the HIL platform.

CRediT authorship contribution statement

Xinmiao Chen: Writing – review & editing, Writing – original draft, Validation, Methodology, Data curation, Conceptualization; **Yuan Yao:** Writing – review & editing, Software, Funding acquisition; **Haifeng Xie:** Validation, Software, Investigation.

Declaration of competing interest

The authors declare that they have no known competing financial interests or personal relationships that could have appeared to influence the work reported in this paper.

Acknowledgment

This work was supported by the National Natural Science Foundation of China (Grant Nos. 52372403 and U2268211), the National Railway Group Science and Technology Program (Grant No. N2025J026), the CRRC Original Technology Ten-Year Cultivation Special Project (2025CYY002), Science and Technology Research and Development Plan Project of CRRC Group Co., Ltd. (2026CTA016), and the Independent Project of the State Key Laboratory of Rail Transit Vehicle System (2026RVL-T04).

References

Achnib, A., & Sename, O. (2023). Discrete-time multi-model preview control: Application to a real semi-active automotive suspension system. *Control Engineering Practice*, *137*, 105553. https://doi.org/10.1016/j.conengprac.2023.105553

Chen, D., Shen, G., & Zong, C. (2018). Analysis of ride quality of railway vehicle based on coupling degree. *Journal of Tongji University (Natural Science)*, *46* (1), 118–124. https://doi.org/10.11908/j.issn.0253-374x.2018.01.017

Chen, X., Yao, Y., Su, H., & Qiao, J. (2026). Modeling and TF-BPNN inverse modeling of a magnetorheological damper. *Journal of Vibration and Control*, *31* (13–14), 2538–2549. https://doi.org/10.1177/10775463261420711

CJJ/T 96-2018 (2018). Standard for metro gauges. Ministry of Housing and Urban-Rural Development of the People's Republic of China.

Fu, B., & Bruni, S. (2022). An examination of alternative schemes for active and semi-active control of vertical car-body vibration to improve ride comfort. *Proceedings of the Institution of Mechanical Engineers, Part F: Journal of Rail and Rapid Transit*, 386–405. https://doi.org/10.1177/09544097211022108

Fu, B., Di Gialleonardo, E., Liu, B., & Bruni, S. (2024). *Modelling, hardware-in-the-loop tests and numerical simulation of magneto-rheological semi-active primary suspensions in a railway vehicle* (vol. 62). Taylor & Francis. https://doi.org/10.1080/00423114.2023.2239391

GB/T 5599-2019 (2019). Specification for dynamic performance assessment and testing verification of rolling stock. State Administration for Market Regula1309 tion of the People's Republic of China and Standardization Administration of the People's Republic of China

Ghoniem, M., Awad, T., & Mokhiamar, O. (2020). Control of a new low-cost semi-active vehicle suspension system using artificial neural networks. *Alexandria Engineering Journal*, 4013–4025). https://doi.org/10.1016/j.aej.2020.07.007

Guo, K., & Wang, Y. (2019). A study on modified acceleration-driven damping control strategy for semi-active suspension. *Automotive Engineering*, *41* (5), 481–486. https://doi.org/10.19562/j.chinasae.qcgc.2019.05.001

Jiang, P., Ling, L., Zhao, J., & Zhai, W. (2025). Experimental and numerical study on bogie hunting motion of metro vehicles induced by wheel concave wear. *Vehicle System Dynamics*, *63* (5), 920–943. https://doi.org/10.1080/00423114.2024.2362942

Jiang, X., Chen, T., Xiong, X., Zeng, J., Zhao, Y., Chen, R., Hao, W., & Cheng, T. (2024). The self-tuning fuzzy sliding mode control method for the suspension system with the LSTM network road identification. *Journal of Sound and Vibration*, *581*, 118401. https://doi.org/10.1016/j.jsv.2024.118401

Jin, T., Liu, Z., Sun, S., Ren, Z., Deng, L., Ning, D., Du, H., & Li, W. (2020). Theoretical and experimental investigation of a stiffness-controllable suspension for railway vehicles to avoid resonance. *International Journal of Mechanical Sciences*, *187*, 105901. https://doi.org/10.1016/j.ijmecsci.2020.105901

Kim, J., Lee, T., Kim, C.-J., & Yi, K. (2023). Model predictive control of a semi-active suspension with a shift delay compensation using preview road information. *Control Engineering Practice*, *137*, 105584. https://doi.org/10.1016/j.conengprac.2023.105584

Lee, D., Jin, S., & Lee, C. (2023). Deep reinforcement learning of semi-active suspension controller for vehicle ride comfort. *IEEE Transactions on Vehicular Technology*, *72* (1), 327–339. https://doi.org/10.1109/TVT.2022.3207510

Li, W., Qi, Y., Wen, Z., Chi, M., Wang, H., Li, X., Zhang, X., & Sun, J. (2025). Coupling effect of track irregularity and wheel–rail contact conicity on carbody swaying of a metro vehicle: An experimental investigation. *Vehicle System Dynamics*, *63* (5), 944–963. https://doi.org/10.1080/00423114.2024.2362947

Liu, P., Zheng, M., Ning, D., Zhang, N., & Du, H. (2022). Decoupling vibration control of a semi-active electrically interconnected suspension based on mechanical hardware-in-the-loop. *Mechanical Systems and Signal Processing*, 108455. https://doi.org/10.1016/j.ymssp.2021.108455

Liu, Y., & Zuo, L. (2016). Mixed skyhook and power-driven-damper: A new low-jerk semi-active suspension control based on power flow analysis. *Journal of Dynamic Systems, Measurement, and Control*. https://doi.org/10.1115/1.4033073

Lu, Y., Khajepour, A., Hajiloo, R., Korayem, A. H., & Zhang, R. (2023). A new integrated skyhook-linear quadratic regulator coordinated control approach for semi-active vehicle suspension systems. *Journal of Dynamic Systems, Measurement, and Control*. https://doi.org/10.1115/1.4056442

Ma, X., Wong, P. K., & Zhao, J. (2019). Practical multi-objective control for automotive semi-active suspension system with nonlinear hydraulic adjustable damper. *Mechanical Systems and Signal Processing*, *117*, 667–688. https://doi.org/10.1016/j.ymssp.2018.08.022

Morselli, R., & Zanasi, R. (2008). Control of port Hamiltonian systems by dissipative devices and its application to improve the semi-active suspension behaviour. *Mechatronics*, *18* (7), 364–369. https://doi.org/10.1016/j.mechatronics.2008.05.008

Pisarski, D., & Jankowski, L. (2024). Decentralized modular semi-active controller for suppression of vibrations and energy harvesting. *Journal of Sound and Vibration*, *577*, 118339. https://doi.org/10.1016/j.jsv.2024.118339

Savaresi, S. M., & Spelta, C. (2007). Mixed sky-hook and ADD: Approaching the filtering limits of a semi-active suspension. *Journal of Dynamic Systems, Measurement, and Control*, *129* (4), 382–392. https://doi.org/10.1115/1.2745846

Shi, H., Zeng, J., & Guo, J. (2024). Disturbance observer-based sliding mode control of active vertical suspension for high-speed rail vehicles. *Vehicle System Dynamics*, *62* (11), 2912–2935. https://doi.org/10.1080/00423114.2024.2305296

Shi, Y., Dai, H., Wang, Q., Wei, L., & Shi, H. (2020). Research on low-frequency swaying mechanism of metro vehicles based on wheel-rail relationship. *Shock and Vibration*, 1–15. https://doi.org/10.1155/2020/8878020

Soliman, A., & Kaldas, M. (2021). Semi-active suspension systems from research to mass-market – a review. *Journal of Low Frequency Noise, Vibration and Active Control*, 1005–1023. https://doi.org/10.1177/1461348419876392

Wang, Z., Guo, Y., & Pan, P. (2026). A novel frequency-domain control strategy for semi-active suspensions with reduced hardware demands. *Mechanical Systems and Signal Processing*, *242*, 113600. https://doi.org/10.1016/j.ymssp.2025.113600

Wu, Y., Gan, F., Shi, H., Zeng, J., Chen, C., & Feng, Y. (2023). Experimental investigations on the semi-active control of a valve-driven secondary lateral damper for a high-speed rail vehicle. *Journal of Vibration and Control*, *29* (13–14), 3025–3037. https://doi.org/10.1177/10775463221090322

Yang, S., Zhao, Y., Liu, Y., Liao, Y., & Wang, P. (2023). A new semi-active control strategy on lateral suspension systems of high-speed trains and its application in HIL test rig. *Vehicle System Dynamics*, *61* (5), 1317–1344. https://doi.org/10.1080/00423114.2022.2081221

Zhang, C., Kordestani, H., & Shadabfar, M. (2023a). A combined review of vibration control strategies for high-speed trains and railway infrastructures: Challenges and solutions. *Journal of Low Frequency Noise, Vibration and Active Control*, 272–291. https://doi.org/10.1177/14613484221128682

Zhang, X. G., Zhou, Y., & Jiang, C. (2023b). Modeling and simulation of lateral fuzzy control semi-active suspension system for high-speed trains considering time delay compensation. *Journal of Railway Science and Engineering*, *20* (4), 1189–1199. https://doi.org/10.19713/j.cnki.43-1423/u.t20220794

Zhang, Y., & Chen, C. (2025). A new mixed skyhook-backstepping semi-active control approach for high-speed train magnetorheological suspension. *Journal of the Brazilian Society of Mechanical Sciences and Engineering*, *47* (7). https://doi.org/10.1007/s40430-025-05662-2

Zhu, W.-Q., & Ying, Z.-G. (2013). Advances in research on nonlinear stochastic optimal control of quasi-Hamiltonian systems. *Advances in Mechanics*, *43* (1), 39–55. https://doi.org/10.6052/1000-0992-12-045

Zolotas, A. C., & Goodall, R. M. (2018). New insights from fractional order skyhook damping control for railway vehicles. *Vehicle System Dynamics*, 1658–1681. https://doi.org/10.1080/00423114.2018.1435889

Zong, L.-H., Gong, X.-L., Xuan, S.-H., & Guo, C.-Y. (2013). Semi-active h∞ control of high-speed railway vehicle suspension with magnetorheological dampers. *Vehicle System Dynamics*, 600–626. https://doi.org/10.1080/00423114.2012.758858